APOE4-induced patterned behavioral decline and neurodegeneration requires endogenous tau in a *C. elegans* model of Alzheimer's disease

Eric A. Cardona[1], Zheng Wu[1], Blythe M. Bolton[2], Elif Sarinay Cenik[2], Jonathan T. Pierce[1]

[1]Department of Neuroscience, Center for Learning and Memory, University of Texas at Austin, Austin, TX

[2]Department of Molecular Biosciences, University of Texas at Austin, Austin, TX

* For correspondence: jonps@utexas.edu

ORCID for Jonathan T. Pierce: 0000-0002-9619-4713

Abstract

Alzheimer's disease (AD) causes a characteristic spatiotemporal pattern of neurodegeneration, resulting in the loss of associated faculties such as cognition. The factors which account for this pattern of degeneration are unclear, as AD risk genes are numerous and often broadly expressed. Previously, we generated a model of AD using the nematode *Caenorhabditis elegans* in which the AD risk variant of apolipoprotein E, *APOE4*, is pan-neuronally expressed. We showed that HSN class motor neurons degenerate in early adult. Here, we expand on our past work by performing behavioral analyses to deduce the effect of APOE4 on the function of distinct neuronal circuits. We found evidence that APOE4 induces dysfunction of other neurons; this spatiotemporal pattern of degeneration roughly correlates with endogenous levels of PTL-1, the *C. elegans* homolog of human MAPT also known as tau. Moreover, deletion of *ptl-1* suppressed defects in multiple behaviors, suggesting broad protective effects across the nervous system including the HSN neurons. Lastly, we show that PTL-1 in the touch receptor neurons, where PTL-1 is most abundant, is required cell nonautonomously for degeneration of the HSN neurons. Our results suggest that *C. elegans* may provide a useful *in vivo* system to study how endogenous Tau acts downstream of APOE4 to cause progressive, patterned neurodegeneration.

Introduction

Neurodegenerative disorders such as Alzheimer's disease (AD), Parkinson's disease (PD), and frontotemporal lobar dementia (FTLD) present with characteristic spatiotemporal patterns of neuronal cell death (Braak and Braak, 1991; Bahia et al., 2013; Reviewed in Rietdijk et al., 2017). Degeneration in characteristic brain regions corresponds to loss of brain region-associated faculties, such as memory in AD (Rosen et al., 2005). Genetic risk factors have been previously associated with AD. Among them, the ε4 variant of Apolipoprotein E (APOE4) is the most common genetic risk factor for earlier onset and faster progression of sporadic AD and AD-like pathology in individuals with Down syndrome (Larsen et al. 2024; Serrano-Pozo et al., 2021). A recent study proposed that *APOE4* homozygosity itself may be a single-gene driver of AD, akin to mutation of the familial AD genes *APP*, *PSEN1*, and *PSEN2* (Fortea et al., 2024; Ryan and Rossor, 2010). Moreover, APOE4 has been shown to increase the severity of other neurodegenerative diseases such as PD and FTLD (Robinson et al., 2018; Koriath et al., 2019; Davis et al., 2020). How APOE4 worsens neurodegeneration (as in AD, PD, and FTLD) or, more interestingly, may induce it (as suspected in AD) and contribute to patterned degeneration is unclear.

As *APOE4* homozygosity alone may cause AD, it is critical to understand how APOE4 contributes to patterned neurodegeneration. One hypothesis is APOE4-induced neurodegeneration follows a spatiotemporal pattern determined by cellular levels of specific vulnerability factors. Multiple lines of evidence suggest that the microtubule associated protein gene, *MAPT*, which encodes tau, represents one such vulnerability factor. First, pathogenic tau forms intracellular aggregates and their accumulation is closely linked to neuronal dysfunction in AD and other degenerative disorders termed tauopathies (Trojanowski et al., 1993; Lin et al., 2019). Second, Tau-related pathology is highly correlated with neurodegeneration according to Braak Staging, a well-established metric of how AD progresses with age (Braak and Braak, 1991; Köpke et al., 1993; Ghoshal et al., 2002). Third, transgenic expression of pathological tau is sufficient to cause neurodegeneration (Mocanu et al., 2008; Spittaels et al., 1999;

55 www.alzforum.org/research-models). Fourth, depletion of endogenous tau mitigates cellular
56 correlates of AD pathology in rodent models of AD which overexpress human *APP* (Roberson et
57 al., 2007; Vossel et al., 2010) or human tau with aggregate-inducing mutations (Wegmann et al.,
58 2015; DeVos et al., 2017). Fifth, growing evidence suggests that pathogenic tau protein can
59 spread in a trans-synaptic fashion between brain regions *in vivo* with age (Liu et al., 2012; de
60 Calignon et al., 2012; Iba et al., 2013; Fu et al., 2016; Meisl et al., 2021; Cornblath et al., 2021).
61 Altogether, these and many other studies provide strong evidence for tau as a candidate
62 vulnerability factor underlying patterned neurodegeneration. Progress has been made to
63 uncover the relationship between APOE4, tau, and neurodegeneration (Shi et al., 2017;
64 Therriault et al., 2020; Seo et al., 2023; Koutsodendris et al., 2023), but whether APOE4 is a
65 causative factor in the pathogenic spread of tau or how APOE4 may contribute to a combination
66 of cell autonomous and non-cell autonomous processes is less clear. Additionally, because
67 rodent models of AD often do not fully recapitulate the neurodegeneration observed in human
68 patients, the cellular molecular bases for this critical pathological phenotype remain have yet to
69 be uncovered.
70 The nematode *Caenorhabditis elegans* has been famously leveraged to discover
71 conserved *in vivo* mechanisms of cell death (Horvitz, 2003). It also represents a potentially
72 useful system to study the cellular molecular bases for patterned neurodegeneration *in vivo*. To
73 model neurodegeneration, past studies have overexpressed human disease genes and
74 investigated the health and function of specific neurons *in vivo* (Faber et al., 1999; Baskoylu et
75 al., 2018; van Ham et al., 2008; Vaccaro et al., 2012b). In transgenic *C. elegans* models,
76 progress has been made to investigate genes involved with AD, notably *MAPT* and *APP*
77 (Kraemer et al., 2003; Treusch et al., 2011; Fatouros et al., 2012; Benbow et al., 2020; Sae-Lee
78 et al., 2020). A powerful feature of *C. elegans* as a model organism is that each one of its 302
79 neurons is identifiable. However, previous studies did not take full advantage of this to
80 investigate whether specific neurons differ in vulnerability due to tau. Thus, the potential of *C.*
81 *elegans* to test spatiotemporal patterns of neurodegeneration remains underutilized.

82 Here, we found that APOE4 induces a spatiotemporal pattern of neurodegeneration in *C.*
83 *elegans* as inferred through the assessment of behaviors which reflect the activity of known
84 neurons. The pattern of neurodegeneration we observed roughly correlates with the neuronal
85 expression levels of *ptl-1*. Complementing our indirect approach, we observed directly via live
86 microscopy that APOE4 causes progressive, age-related HSN axon dysmorphia coincident with
87 dysfunction of that neuron. Deletion of *ptl-1* suppressed both APOE4-induced behavioral
88 defects and HSN axon dysmorphia. Genetic ablation of the mere six neurons most enriched
89 with PTL-1—the touch receptor neurons (TRNs)—similarly suppressed HSN dysfunction; this
90 was phenocopied by targeted depletion of PTL-1 in the TRNs. These results suggest a non-cell
91 autonomous role for PTL-1 in APOE4-induced degeneration. Overall, our findings position the
92 APOE4 worm model as a useful system to study how endogenous tau/PTL-1 participates in the
93 cellular molecular mechanisms underlying patterned neurodegeneration. This may aid in the
94 development of new therapeutic measures against tauopathies, such as AD.
95
96 **Results**
97 **APOE4 induces progressive, widespread behavioral defects in *C. elegans***
98 Our previous study using *C. elegans* showed that pan-neuronal expression of *APOE4* induced
99 degeneration of a subset of neurons (the HSN pair) in early adult, while others (such as VA and
100 VB class neurons) appeared to remain healthy (Sae-Lee et al., 2020). To expand on this study,
101 we investigated whether APOE4 induces a wider pattern of neurodegeneration. We assayed a
102 variety of behaviors to assess the function of different subsets of neurons. We reasoned that we
103 could deduce the health and function of different neuronal subsets and circuits by measuring the
104 performance of these behaviors.
105 We selected seven different behaviors that rely primarily, but not exclusively, on mostly
106 distinct subsets of identified neuron classes (Fig. S1). Five behaviors we tested—*egg laying*,
107 *pharyngeal pumping*, *gentle* and *harsh touch response*, and *locomotor gait transition*—have
108 specific neurons which are critical for behavioral execution. These include: the HSN class

109 neurons for egg laying behavior (Schafer, 2005); the MC and M3 neurons for pumping of the
110 pharyngeal feeding organ (Avery and You, 2012); the six touch receptor neurons (TRNs) for
111 gentle touch response (Chalfie and Sulston, 1981; Chalfie et al., 1985); the FLP and PVD
112 neurons, with lesser contribution from redundant mechanoreceptive neurons and interneurons,
113 for harsh touch response (Li et al., 2011); and lastly, the ADE and PDE dopaminergic neurons
114 for the transition between swim and crawl locomotor gaits (Vidal-Gadea et al., 2011). We also
115 assessed two readouts of locomotor behavior that rely on many more neurons with partial
116 redundancy. *Short-term locomotion* relies on over 100 motor neurons and about one dozen pre-
117 motor interneurons; *long-term locomotion* relies on those neurons and additional sensory
118 neurons and interneurons to mediate switches between roaming and dwelling states (Flavell, et
119 al., 2020).

120 We evaluated behavioral performance at adult days 1 through 5 (D1-5) (Fig. 1A, left).
121 This age range encompasses the peak reproductive period when *C. elegans* is active across a
122 range of behaviors and lays eggs (Scharf et al., 2021). We refer to “age of onset” of behavioral
123 decline as the first day of the adult stage that APOE4 worms displayed significantly impaired
124 behavior compared to age-matched controls.

125 Over the course of D1-5 of adult, we found that APOE4 worms displayed differences in
126 all seven behaviors compared to control (Fig. 1B-H). In as early as D1 adults, gentle touch
127 sensitivity, pharyngeal pumping, and short-term locomotion performances decreased by 11%,
128 13%, and 24%, respectively; gait transition decreased by a marked 59% (Fig. 1B-E). In D2
129 adults, long-term locomotion showed a 12% decline. We also replicated our previous finding of
130 an egg-laying defect which leads to larvae hatching internally, a salient phenotype called
131 “bagging” (Sae-Lee et al., 2020; Fig. 1G). APOE4 worms showed a salient 60% incidence of
132 bagging, peaking at D3. Whereas other behavioral performances declined, harsh touch
133 sensitivity oddly increased in APOE4 worms relative to control beginning at D3 (Figs. 1H, S2).
134 Altogether, these results indicate that APOE4 induces age-related abnormalities in multiple
135 behaviors which primarily rely on distinct subsets of neurons. From this observation, we

136 conclude that the APOE4 worm exhibits a wider spatiotemporal pattern of neurodegeneration,
137 beyond the HSN neuron pair, across early worm adult age.

138 **APOE4-induced progressive behavioral defects require the worm ortholog of tau**

139 Above, we reported that gentle touch response is among the first behaviors to decline
140 with APOE4 on D1 adult. This behavior is mediated by the six touch receptor neurons (TRNs)
141 which feature a prominent array of microtubules that were exploited to discover the first
142 microtubule gene (Chalfie and Thomson, 1979; Chalfie and Thomson, 1982). Studies have
143 shown that tau binds to and stabilizes neuronal microtubules in mammals (Butner and
144 Kirschner, 1991; Santarella et al., 2004). As one may expect from microtubule-enriched
145 neurons, the worm homolog of tau, PTL-1, is highly enriched in the TRNs compared to other
146 neurons, notably the PLM and ALM classes, according to recent single-cell transcriptomic
147 analyses (Taylor et al., 2021; Roux et al., 2023; Fig. S3). We also noticed a rough correlation
148 between endogenous levels of PTL-1 in specific neurons across the nervous system and the
149 age of onset for APOE4-induced behavioral decline. This is represented in Fig. S1, where gray
150 shows what fraction of ptl-1 is expressed in critical neurons that subserve each behavior. Given
151 that tau represents a pathological hallmark associated with neurodegeneration in AD, we
152 speculated that the high endogenous levels of PTL-1 in the TRNs may explain the early onset
153 for the APOE4-induced gentle touch defect. Following this idea, we also hypothesized that
154 deletion of *ptl-1* may confer neuroprotection against APOE4. Into an APOE4 background we
155 crossed a *ptl-1* mutant bearing the *ok621* deletion allele (Δ*ptl-1*). This allele represents a strong
156 hypomorph, if not a null allele, as it lacks four exons that encode conserved microtubule-binding
157 domains important for PTL-1 function (Goedert et al., 1996; Gordon et al., 2008; Hashi et al.,
158 2015; Figs. 1A right, S4).

159 We found that deletion of *ptl-1* significantly suppressed APOE4-induced defects in four
160 out of seven behaviors. We observed complete suppression of defects in gentle touch and
161 pharyngeal pumping (Fig. 1B,C), with partial suppression for defects in gait transition and egg

162 laying (Fig. 1D,G). We did not observe suppression of APOE4-induced abnormalities in short-
163 and long-term locomotion nor for harsh touch sensitivity (Fig. 1E,F,H).
164 The behavioral performance of the *ptl-1* null mutant was also indistinguishable from
165 control across six out of seven behaviors. Although the *ptl-1* null mutant displayed a moderate
166 defect in swim-to-crawl transition compared to control, the *ptl-1* null mutant nonetheless partially
167 suppressed the defect induced by APOE4 as opposed to additively worsening the defect (Fig.
168 1D). Also, although *ptl-1* deletion led to a non-significant trend toward lower bagging compared
169 to control animals, it caused a significant suppression of the APOE4-induced bagging (Fig. 1G).
170 Altogether, we conclude that PTL-1 broadly contributes to the neuronal dysfunction
171 given significant and multiple behavior changes observed in the presence of APOE4.
172 **APOE4-induced degeneration of HSN axon requires worm ortholog of tau**
173 Previously, we showed that APOE4-induced bagging coincided with degeneration of the
174 bilaterally symmetric pair of HSN egg-laying motor neurons (Sae-Lee et al., 2020). Because
175 deletion of *ptl-1* suppressed APOE4-induced bagging, we hypothesized that *ptl-1* deletion would
176 also suppress HSN neurodegeneration. To test this, we inspected the health of reporter-labeled
177 HSN neurons in live worms with epifluorescent microscopy. Dorsal to the vulva, which is the
178 egg-laying orifice, the HSNs are situated in the midbody of the worm (depicted in Fig. 2A). To
179 quantify degeneration, we initially calculated various metrics of HSN soma geometry and
180 reporter intensity across strains (Fig. S5A), focusing on D3 adult animals which is the age of
181 onset for increased bagging (~70% incidence in APOE4 worms; Fig. 1G).
182 Consistent with our previous study (Sae-Lee et al., 2020), we found that the HSN soma
183 appeared on average much dimmer in APOE4 than control worms, indicative of degeneration
184 (Fig. S5D). However, deletion of *ptl-1* alone also appeared to have caused dimming along with
185 abnormally large appearance of the HSN soma (Fig. S5B,D). We found no straightforward
186 relationship between other soma morphometrics and HSN dysfunction as reflected by bagging
187 incidence across control, *ptl-1*, and APOE4 strains (compare Fig. 1G to Fig. S5 measures).
188 Thus, we conclude that HSN soma geometry and brightness are inconsistent predictors of HSN

189 function in these strains. possibly due to unforeseen aspects of the fluorescent reporter (see
190 Methods).

191 Seeking a more reliable cellular correlate of HSN function, we next investigated HSN
192 axon morphology. Previous work using laser ablation and mutants showed the proximal axon
193 portion (located between soma and vulval muscles)—but not distal portion which continues
194 anteriorly—is required for egg laying behavior (Garriga et al., 1993; Fig. 2A). Therefore, we
195 hypothesized that morphology of the proximal axon may serve as a useful correlate of HSN
196 neuron function.

197 We visualized the HSN proximal axon with the same fluorescent reporter as above for
198 the soma. The ~11 µm-long HSN proximal axon typically comprises two segments joined at a
199 right-angle (Fig. 2B image 1). The initial segment, which is qualitatively thicker, projects
200 anteriorly from the soma (segment i.) before turning ventrally at a right-angle into a second,
201 thinner segment (segment ii.) that joins the ventral nerve cord (VNC) and branches dorsally to
202 innervate egg-laying musculature. The unbranched, distal axon continues anteriorly within the
203 VNC to the head (Fig. 2A; Garriga et al., 1993). In our control reporter strain, we found that
204 ~58% of worms had a proximal axon with this typical two-segment, right-angle morphology
205 (N=93; Fig. 2B image 1), while the remainder had a single ventrally-projecting proximal axon
206 from the soma (Fig. 2B image 2). The latter single-segmented axons were thin and resembled
207 segment ii. of two-segment HSN proximal axons. We speculate that the thicker, anteriorly
208 directed segment i. did not develop in these worms because the HSN soma had already
209 migrated to a position directly dorsal from the vulval muscles. Although the HSN proximal axon
210 has been previously depicted with two segments connected at a right angle (Asakura et al.,
211 2007; Tsutsui et al., 2021), both configurations have been described in the literature and are
212 functional (Garriga et al., 1993). Thus, both types of proximal axons were scored as normal.

213 To check for axon abnormalities potentially caused by APOE4, we next qualitatively
214 scored the morphology of HSN proximal axons and quantified their lengths in D3 adult animals.
215 We found that the incidence of abnormal proximal axons was more than double in APOE4

216 compared to control worms. Proximal axons often took eccentric, elongated paths in APOE4
217 worms (compare Fig. 2B normal images 1,2 to abnormal images 3-10). This was not easily
218 explained by abnormal positioning of the HSN soma, as the somas were similarly located in
219 both APOE4 and control worms; soma positions were quantified as the HSN soma to VNC
220 distance and the HSN soma to vulva area distance (Fig. S6C left) or the angle formed between
221 these two vectors (Fig. S6C right; Asakura et al., 2007).

222 We observed at least three distinct qualitatively abnormal morphologies of the proximal
223 axons relative to control. First, segment i. (Fig. 2B, image 3) or segment ii. (Fig. 2B, image 4)
224 had an extra ~90-degree turn. Second, segment i. connected to segment ii. with a typical right-
225 angle turn, but displayed an atypical ~45-degree portion, with an apparently wider segment near
226 the soma (Fig. 2B images 5,6). Third, segments i. and ii. together took on a hook-like shape
227 oriented anteriorly (Fig. 2B images 7,8). We also noted additional cases (<5% frequency) where
228 these morphological abnormalities appeared to co-occur (e.g., segment ii. extra right-angle turn
229 and segment i. 45-degree portion, Fig. 2B, image 10). Overall, we conclude that APOE4
230 appears to induce a variety of proximal axon abnormalities of the HSN neurons.

231 To help distinguish whether the HSN proximal axon abnormality represented a
232 developmental defect, age-related degeneration, or both, we inspected younger adult animals to
233 determine when the defect started. By at least D1, there was a non-significant trend toward
234 increased abnormal axons in APOE4 worms versus control (Fig. 2C). However, in D3 adults,
235 the percentage of abnormal axons showed a significant three-fold increase in APOE4 worms
236 versus control (Fig. 2D). From these observations, it appears that the proximal axon defect
237 begins by at least D1 in some APOE4 worms but progresses in an age-related fashion,
238 concurrent with the age of onset for increased bagging (Fig. 1G). We thus conclude that the
239 increased incidence in axon abnormality primarily reflects degeneration.

240 We next tested whether deletion of *ptl-1* might suppress APOE4-induced abnormal HSN
241 proximal axon morphology. To partly control for genetic background, we inspected two
242 independent isolates of APOE4;Δ*ptl-1* worms that were crossed with the HSN reporter strain.

243 For both isolates, we found that the *ptl-1* deletion suppressed the APOE4-induced abnormal
244 axon morphology (Fig. 2D). Moreover, although the incidence of axon abnormality was slightly
245 higher in the *ptl-1* deletion mutant at D1, the axon defect was nonetheless significantly
246 suppressed by *ptl-1* deletion in D3 adults (Fig. 2C,D).

247 The above results support the idea that normal proximal HSN axon morphology is a
248 reliably predictive correlate of efficient egg-laying behavior and thus HSN health and function.
249 Specifically, the similar incidence of axon abnormality and bagging in APOE4 worms led us to
250 conclude that abnormal proximal axons reflect a defect in HSN function (compare control to
251 APOE4 in Figs. 1G, 2D). Finally, we found that deletion of *ptl-1* is protective against age-related
252 APOE4-induced defects in behavioral performance as well as HSN proximal axon morphology.

253 **Ablating tau-rich touch receptor neurons protects HSN from APOE4-induced dysfunction**

254 The spatiotemporal pattern of degeneration in AD is thought to be partly explained by
255 pathological forms of tau spreading between connected neurons and across the brain (intra-
256 and extra-synaptically; Liu et. al, 2012; de Calignon et al., 2012). As shown above, the systemic
257 deletion of *ptl-1* protected against age-related APOE4-incuded behavioral defects and abnormal
258 HSN proximal axon morphology. We next sought to test whether PTL-1 might contribute non-
259 cell autonomously to degeneration, explaining in part the spatiotemporal pattern of degeneration
260 in our APOE4 worm model. We hypothesized that targeting the most PTL-1-abundant neurons
261 which— tend to become dysfunctional early—may suppress the degeneration of other neurons
262 that express PTL-1 at a lower level and become dysfunctional later. The TRNs represent the
263 neuronal class most abundant in PTL-1 in *C. elegans*. Over 30% of neuronal *ptl-1* transcripts
264 are expressed in the mere six TRNs (Fig. S1,S3; Taylor et al., 2021; Roux et al., 2023).
265 Coincidentally, the TRNs also become dysfunctional in D1 adults (Fig. 1B). In contrast, the HSN
266 neurons express ~80% less *ptl-1* than the TRNs and become dysfunctional later starting in D3
267 adults (Figs. 1G, S3; Taylor et al., 2021). Some TRNs are also nearby the HSN neurons, such
268 as the PLMs which synapse onto the HSN neurons (White et al., 1986). Thus, the TRNs and

269 HSN neurons in worm offer a convenient platform to test whether PTL-1 contributes non-cell
270 autonomously to degeneration.

271 To assess the TRNs and PTL-1 protein *in vivo* during our targeted manipulations, we
272 took advantage of a control strain in which endogenous PTL-1 protein translationally tagged
273 with mNeonGreen (PTL-1::mNG; Krieg, et al., 2017). Consistent with transcriptional studies,
274 TRNs were readily visible in living larval and adult stages by their abundant mNG-tagged PTL-1
275 (Representative PLM neuron in Figs. 3A2,4B2). We also tested whether the mNG tag on PTL-1
276 impedes its apparent neurotoxic properties downstream of APOE4. If this were the case, we
277 might expect less HSN dysfunction in APOE4;PTL-1::mNG worms. Instead, we found bagging
278 incidence in APOE4;PTL-1::mNG worms (60%) was similar to that of the APOE4-alone strains
279 generated in the current (~70%) and our previous (50-60%) studies (note: all APOE4 strains
280 depicted in Fig. 3A1 express mNG::PTL-1, versus those in Fig. 1G which do not; Sae-Lee et al.,
281 2020). We conclude that the endogenous mNG tag does not interfere with the presumed toxicity
282 of PTL-1 in an APOE4 background.

283 For our first targeted manipulation, we tested whether ablation of the TRNs suppresses
284 APOE4-induced HSN dysfunction. To do this, we leveraged the apoptotic trigger EGL-1, the
285 sole worm homolog of the human BH3-only domain proteins BAM and BID. Targeted
286 expression of *egl-1* has been previously used to kill specified cells (Chang et al., 2006). To kill
287 the TRNs, we generated a strain whose *egl-1* expression is driven by the promoter of *mec-17*, a
288 gene expressed exclusively in the TRNs (TRNs::EGL-1; Wu et al., 2025). The TRNs::EGL-1
289 strain was then crossed into the mNG-tagged *ptl-1* genetic background. To confirm the efficacy
290 of TRN genetic ablation, we took advantage of the relative abundance of mNG-tagged PTL-1 in
291 the TRNs (Fig. S3), which could be directly observed using epifluorescence microscopy (Fig.
292 3A2 control). Anatomically, this was easier to test with the PLM class of TRNs due to how its
293 soma and process are confined in the narrow tail region, in contrast with the other TRN classes
294 with soma situated in the thicker midbody (Fig. 3A2 control; WormAtlas). We found that 93% of
295 TRNs::EGL-1 animals had no detectable PTL-1::mNG where PLM soma and processes were

296 expected compared to control (N=46; Fig. 3A2), suggesting a successful cell ablation in most
297 cases.

298 We found that ablating the TRNs partially suppressed APOE4-induced HSN dysfunction
299 as indicated by a ~30% reduction in bagging incidence (yellow bar, Fig. 3A1). Ablation of the
300 TRNs alone in the control strain had no effect on bagging (white bar, Fig. 3A1). Impressively,
301 ablating the TRNs conferred a similar magnitude of protection as afforded by systemic deletion
302 of *ptl-1* (compare blue bar in Fig. 1G to yellow bar in Fig. 3A1). Thus, we deduce that TRNs
303 activity and/or their cellular contents may contribute non-cell autonomously to APOE4-induced
304 HSN degeneration.

305 Because TRN activity is obviously lost after genetic ablation, we asked whether simply
306 blocking TRNs function alone as opposed to whole cell ablation may protect the HSNs against
307 APOE4. We tested this by using a deletion allele of *mec-4*, a gene which encodes
308 mechanoreceptive DEG/ENaC channel expressed predominantly in the TRNs (Chalfie and
309 Sulston, 1981). We took advantage of the *u253* loss-of-function allele of *mec-4*, referred hereon
310 as *mec-4*(*lf*), which abolishes transduction of mechanosensory currents and gentle touch
311 response yet leaves the TRNs otherwise physiologically and morphologically normal (O'Hagan,
312 et al., 2005). We found that *mec-4*(*lf*) failed to suppress APOE4-induced HSN dysfunction (Fig.
313 3B). We conclude that functional impairment of the TRNs is insufficient to protect HSNs against
314 APOE4.

315 **Targeted reduction of tau in touch receptor neurons protects HSN against APOE4**

316 Because the worm ortholog of tau, PTL-1, is especially abundant in the TRNs (green
317 bars in Fig. S3), we hypothesized that targeted depletion of PTL-1 contained in the TRNs would
318 protect against APOE4-induced HSN dysfunction, phenocopying TRNs ablation. To test this, we
319 knocked down *ptl-1* expression in the TRNs using cell-selective RNAi as previously described
320 (TRNs::*ptl*-1 KD; Esposito et al., 2007). To determine the efficacy and selectivity of the
321 knockdown, we quantified PTL-1::mNG fluorescence intensity in TRN soma versus example
322 non-targeted neurons. Conveniently, the soma of the non-targeted VC4 and VC5 class motor

323 neurons (depicted in Fig. 2A) are also easily detectable by PTL-1::mNG fluorescence.
324 Compared to control, TRNs::*ptl-1* KD worms had an average 40% decrease in PTL-1::mNG
325 fluorescence in five out of the six TRNs (Fig. 4A2). In contrast, PTL-1::mNG fluorescence
326 intensity was unchanged in the non-targeted VC4 and VC5 neurons (Fig. 4A2). These
327 observations suggested an effective and selective knockdown of *ptl-1* in the TRNs.
328 Using this strategy, we found that knockdown of *ptl-1* in the TRNs partially suppressed
329 APOE4-induced HSN dysfunction. This was determined after scoring bagging in two
330 independent isolates of APOE4 worms crossed with the TRNs::*ptl-1* KD strain to partly control
331 for genetic background (blue bars, Fig. 4A1). In contrast, knockdown of *ptl-1* in TRNs alone in
332 the control strain had no effect on bagging (white bar, Fig. 4A1). While significant, the
333 suppressive effect was noticeably weaker compared to the systemic *ptl-1* deletion (compare
334 with APOE4;Δ*ptl-1* strain, blue bar in Fig. 1G). We speculated that the weaker suppression may
335 be explained by RNAi reducing only a portion of *ptl-1* transcripts in the TRNs (Fig. 4A2). This
336 prompted us to test whether complete loss of *ptl-1* in the TRNs more strongly suppresses HSN
337 dysfunction than in APOE4;TRNs::*ptl-1* KD worms.
338 To achieve a targeted *ptl-1* knockout in the TRNs, we used an intersectional Cre-LoxP
339 approach. *LoxP* sites were first introduced via CRISPR to flank the endogenous *ptl-1*::*mNG*
340 locus (*LoxP*::*ptl-1*::*LoxP* strain). *LoxP*::*ptl-1*::*LoxP* worms were then crossed with a strain which
341 expresses Cre recombinase under the same TRNs-specific promoter as our TRNs::EGL-1 strain
342 (Harterink et al., 2018; Sanfeliu-Cerdán et al., 2023; Wu et al., 2025). This should result in a
343 selective knockout of *ptl-1* in the TRNs (TRNs::*ptl-1* KO). The efficacy of the *ptl-1* knockout was
344 confirmed by evaluating the presence of PTL-1 in the PLM neurons via PTL-1::mNG
345 fluorescence signal (Fig. 4B2). PTL-1::mNG was absent in 100% of PLM neurons in TRNs::*ptl-1*
346 KO animals (N=45). However, we were unable to detect significant reduction in mNG-tagged
347 PTL-1 protein as evaluated by Western blot probing for the FLAG epitope engineered into the
348 tag (Fig. S7; Krieg et al., 2017).

349 As with the knockdown, we found that knockout of *ptl-1* in the TRNs partially suppressed
350 APOE4-induced HSN dysfunction. This was determined after scoring bagging in two
351 independent isolates of APOE4 worms crossed with the TRNs::*ptl-1* KO strain to partially control
352 for genetic background (blue bars in Fig. 4B1). In contrast to the mild suppression after *ptl-1*
353 knockdown (blue bars in Fig. 4A1), the average extent of suppression by knockout in the TRNs
354 was more equivalent to that of the systemic deletion of *ptl-1* (Fig. 1G).
355 Altogether, these findings suggest that PTL-1 is required in the TRNs to contribute non-
356 cell autonomously to APOE4-induced degeneration of the HSN neurons.
357

358 **Discussion**

359 **APOE4-induced pattern of neurodegeneration in *C. elegans***

360 In this study, we build on our prior work by characterizing APOE4-induced, age-related
361 abnormalities across seven behaviors in a *C. elegans* model of Alzheimer's disease (AD). The
362 pattern of decline provides evidence for spatiotemporal APOE4-induced neurodegeneration.
363 Finally, we demonstrate that endogenous tau contributes to APOE4-induced degeneration and
364 multiple behavioral defects.
365 *C. elegans* has served as a leading model organism to study forms of cell death (Horvitz
366 2003); however, its potential to study *patterned neurodegeneration* in response to human
367 disease genes remains to be explored. This prompted us to ask whether APOE4 worms display
368 a pattern of neurodegeneration beyond the HSN neurons as we previously reported (Sae-Lee et
369 al., 2020). By day 4 (D4) of adulthood, APOE4 worms exhibit defects of varying severity in all
370 seven tested behaviors. Because each behavior primarily relies on mostly distinct subsets of
371 neurons (Fig. S1), this suggests a progressive, neuron-specific pattern analogous to the
372 characteristic progression observed in human AD (Braak and Braak, 1991; Scahill et al., 2002;
373 Fiford et al., 2018). The sensitivity of certain behaviors to decline merits follow up studies to
374 investigate putative higher-vulnerability neurons (e.g., the ADE and PDE neurons required for
375 swim-crawl gait transition; Fig. 1D; Vidal-Gadea et al., 2011). Certain behaviors were not

376 impacted by pan-neuronal APOE4 expression; this may reflect how certain neurons are resilient
377 to PTL-1-mediated degeneration. This idea is mirrored in human AD where brain regions such
378 as the somatosensory cortex and brainstem are similarly spared from degeneration, even in
379 advanced stages of AD (Rondina et al., 2018). Alternatively, apparent resistance to APOE4 may
380 reflect neuronal circuit redundancy. In this vein, the subtle defects we observed in locomotion
381 could reflect the suspected functional redundancy of *C. elegans* motor neurons (Fig. 1E,F;
382 Izquierdo and Beer, 2018). Interestingly, harsh-touch sensitivity subtly *increased* in APOE4
383 worms, hinting at neuronal hyperexcitability (Fig. 1H). In mouse, APOE4-driven hyperexcitability
384 may result from degeneration of inhibitory neurons (Nuriel et al., 2017a). This aligns with fMRI
385 studies of AD patients showing abnormally high activity in certain brain regions (Bookheimer et
386 al., 2000; Tuovinen et al., 2020). Future studies could explore how APOE4 alters excitability of
387 harsh touch neurons (e.g., the PVDs) and how this may correlate with APOE4-induced
388 progressive dysmorphia of the elaborate PVD dendrite arborization (Jiang et al., 2025).
389 Axon dysmorphia, or axonopathy, is a hallmark of AD characterized by neurite
390 deterioration and general white matter abnormalities (Lee et al., 2016). Similar axon defects,
391 sometimes without cell body loss, have been observed in human AD patients and mouse
392 neurodegenerative disease models (Leroy et al., 2007; Yoshiyama et al., 2007; Crespo-Biel et
393 al., 2014). Here, we identified APOE4-induced dysmorphia of the HSN proximal axon (Fig. 2).
394 Our findings suggest this reflects a degenerative phenotype rather than a developmental defect,
395 as egg laying behavior as well as HSN soma position and axon shape are all initially normal in
396 D1 versus D3 adult APOE4 worms (Figs. 2B,C,D, S6). Worm neurons have been shown to
397 contain axonal domains with distinct structures and functions (Mizumoto and Shen, 2013; Eichel
398 et al., 2022). Future studies should consider what molecular factors might render the proximal
399 HSN axon vulnerable to dysmorphia. Overall, the tight correlation between a salient behavioral
400 phenotype (bagging; Fig. 1G) and axon dysmorphia of an identified neuron (HSN; Fig. 2)
401 provides a powerful system to study subcellular mechanisms of APOE4-induced axonopathy.

402 *C. elegans* has become increasingly recognized as a valuable *in vivo* model for studying
403 tau pathology (Reviewed in Natale et al., 2020). Along with extracellular amyloid-β plaques,
404 intracellular tau aggregation is a key pathological hallmark of AD (Kowall and Kosik, 1987; Kosik
405 et al., 1988; Grunke-Iqbal et al., 1986; Lee and Trojanowski, 1992). In AD and other
406 tauopathies, tau undergoes conformational changes that promote aggregation into tangles,
407 driving neurodegeneration (Friedhoff et al., 1998a,b; Jeganathan et al., 2006; Jeganathan et al.,
408 2008; Oakley et al., 2020). Unlike mammals, which have three broad tau-related gene families,
409 the worm has but a single endogenous homolog: *ptl-1* (Sündermann et al., 2016; Goedert et al.,
410 1996; Gordon et al., 2008). We found that deletion of *ptl-1* suppresses APOE4-induced defects
411 in four out of seven tested behaviors—including HSN-associated bagging—*and* HSN axon
412 morphological defects induced by APOE4. This fits with the idea that tau acts as an effector of
413 pathogenic events in AD initiated by APOE4. Indeed, past immunohistochemical evidence
414 suggested that APOE and tau co-localize – and possibly physically interact – in postmortem
415 brain tissue from individuals with Alzheimer's disease (Benzing and Mufson, 1995; Brecht et al.,
416 2004; Zhou et al., 2006; Rohn et al., 2012). Further studies showed that APOE4 expression
417 induces tau aggregates in cultured mouse neurons and worsens tau pathology in an AD mouse
418 model (Huang et al., 2001; Seo et al., 2023; Koutsodendris et al., 2023 Shi et al., 2017). It will
419 be interesting to see whether endogenous worm PTL-1 has similar pathological capacity
420 detectable at the biochemical level.
421 We found that deletion of endogenous *ptl-1* suppresses APOE4-induced degeneration.
422 This parallels a previous report in a mouse AD model in which APOE4-induced dysfunction of
423 specific interneurons was suppressed by knocking out endogenous murine tau (Andrews-
424 Zwilling et al., 2010). Interestingly, another study found that depletion of endogenous tau
425 protected against neurodegeneration in an amyloid-β mouse model (Roberson et al., 2007).
426 Because *C. elegans* lacks an *APP* ortholog whose protein product is capable of generating
427 amyloid-β fragments (Daigle and Li, 1993), the benefits of PTL-1 reduction likely operate
428 independently of amyloid-β. Interestingly, a recent study found that *ptl-1* deletion partly mitigated

429 age-dependent accumulation of pathogenic human Tau upon its overexpression in worm
430 neurons (Nunez et al., 2022). Thus, the APOE4 worm model of AD represents an Aβ-agnostic
431 model to investigate how endogenous tau contributes to patterned degeneration downstream of
432 APOE4.

433 PTL-1 may contribute cell non-autonomously to degeneration in our APOE4 worm
434 model. The touch receptor neurons (TRNs) contain the majority of PTL-1 in the worm nervous
435 system (green bars in Figs. 3A2, 4A2; Taylor et al., 2021; Roux et al., 2023). We found that
436 depleting PTL-1 in the TRNs via genetic ablation, RNAi-mediated knockdown, and Cre-LoxP-
437 mediated knockout all partially suppressed APOE4-induced dysfunction of HSN neurons. Each
438 targeted manipulation roughly matched the magnitude of suppression achieved by systemic *ptl-*
439 *1* deletion. This raises the intriguing possibility that, although *ptl-1* remains widely expressed,
440 PTL-1 from the mere six TRNs is required cell non-autonomously for HSN dysfunction.

441 How might PTL-1 in the TNRs lead to APOE4-induced degeneration of the HSNs? The
442 popular hypothesis that pathological tau spreads across the brain offers a partial link between
443 tau pathology and spatiotemporal neurodegeneration (Braak and Braak, 1991; Reviewed in
444 Braak and Del Tredici, 2011; Frost et al., 2010). Tauopathy mouse models show that
445 pathological tau can propagate across synapses, starting from "seed" regions rich in Tau (and
446 high in inter-neuronal connectivity) and spreading to distant brain regions (Clavaguera et al.,
447 2009; Kfoury et al., 2012; Liu et al., 2012; de Calignon et al., 2012; Iba et al., 2013). Similarly,
448 we hypothesize that pathological PTL-1 may spread from neuron to neuron over time in worm.
449 Although the six TRN soma are relatively distant from the two HSN soma (1/2-1/3 body length
450 or ~30-50 mm), PTL-1 is also enriched in TRN processes which pass nearby the HSNs (Fig.
451 3A2). Two TRNs (the PLM pair) also form chemical synapses with the HSNs (White et al.,
452 1986). Future work could leverage synaptic transmission mutants to test whether this represents
453 a site of PTL-1 spread (Miller et al., 1996; McColluch et al., 2017). If the hypothetical PTL-1
454 spread is synaptic, genetically perturbing TRN neurotransmission may phenocopy our targeted
455 manipulations described above, suppressing HSN dysfunction. Moreover, we found that

456 fluorescently tagged PTL-1 did not interfere with PTL-1-dependent degeneration of the HSNs
457 (compare APOE4 strains with mNG tagged PTL-1 in Figs. 3,4 to non-tagged PTL-1 in Fig. 1G).
458 This raises the possibility of directly visualizing PTL-1 spread *in vivo*. With its simpler and fully
459 mapped nervous system, *C. elegans* offers a simple model to investigate how endogenous tau
460 propagates *in vivo* and contributes to APOE4-induced patterned neurodegeneration.
461

462 **Materials and Methods**

463 **Strain Maintenance**

464 Worms were maintained at room temperature (20 °C) on NGM plates seeded with OP50
465 bacteria as described (Brenner et al. 1974). Strains with extrachromosomal transgenes were
466 propagated using selectable fluorescent reporters. Strains are listed in order of appearance in
467 figures:

468 **Figures 1 and S2**

JPS1451 *vxEx1211[Pmyo-3::mCherry::UNC54UTR]*

RB809 *ptl-1(ok621) III*

JPS1453 *vxEx1213[Prab-3::ND18ApoE4::UNC54UTR + Pmyo-3::mCherry::UNC54UTR]*

JPS1455 *vxEx1215[Prab-3::ND18ApoE4::UNC54UTR + Pmyo-3::mCherry::UNC54UTR]; ptl-1(ok621) III*

Figures 2, S5, and S6

JPS1666 *vxIs591[vxIs591[ptph-1::GFP::unc-54UTR]; vxEx1211[Pmyo-3::mCherry::UNC54UTR]*

JPS1664 *vxIs591[vxIs591[ptph-1::GFP::unc-54UTR]; vxEx1211[Pmyo-3::mCherry::UNC54UTR]; ptl-1(ok621) III*

JPS1667 *vxIs591[vxIs591[ptph-1::GFP::unc-54UTR]; vxEx1213[Prab-3::ND18ApoE4::UNC54UTR + Pmyo-3::mCherry::UNC54UTR]*

JPS1778 *vxIs591[vxIs591[ptph-1::GFP::unc-54UTR]; vxEx1213[Prab-3::ND18ApoE4::UNC54UTR + Pmyo-3::mCherry::UNC54UTR]; ptl-1(ok621) III*

JPS1779 *vxIs591[vxIs591[ptph-1::GFP::unc-54UTR]; vxEx1213[Prab-3::ND18ApoE4::UNC54UTR + Pmyo-3::mCherry::UNC54UTR]; ptl-1(ok621) III*

Figure 3

JPS1571 *vxIs591[vxIs591[ptph-1::GFP::unc-54UTR]*

JPS1828 *vxEx1511[Pmec-17::EGL-1::egl-1UTR]*

TU253 *mec-4(u253) X*

JPS1500 *vxIs824[prab-3::ND18ApoE4::UNC54UTR, pmyo-2::mCherry::UNC54UTR]; ptl-1(pg73[PTL-1::mNeonGreen])*

JPS1839 vx*Is824[prab-3::ND18ApoE4::UNC54UTR, pmyo-2::mCherry::UNC54UTR]; ptl-1(pg73[PTL-1::mNeonGreen]); vxEx1511[Pmec-17::EGL-1::egl-1UTR]*

JPS1709 *vxIs824[prab-3::ND18ApoE4::UNC54UTR, pmyo-2::mCherry::UNC54UTR]; ptl-1(pg73[PTL-1::mNeonGreen]); mec-4(u253) X*

Figure 4

JPS1571 *vxIs591[vxIs591[ptph-1::GFP::unc-54UTR]*

JPS1456 *ptl-1(pg73[PTL-1::mNeonGreen]);vxEx1216[Pmec-17::ptl-1 sense and antisense CDS + Punc-122::RFP]*

JPS1500 *vxIs824[prab-3::ND18ApoE4::UNC54UTR, pmyo-2::mCherry::UNC54UTR]; ptl-1(pg73[PTL-1::mNeonGreen])*

JPS1581 *vxIs824[prab-3::ND18ApoE4::UNC54UTR, pmyo-2::mCherry::UNC54UTR]; ptl-1(pg73[PTL-1::mNeonGreen]); vxEx1216[Pmec-17::ptl-1 sense and antisense CDS + Punc-122::RFP]*

JPS1582 *vxIs824[prab-3::ND18ApoE4::UNC54UTR, pmyo-2::mCherry::UNC54UTR]; ptl-1(pg73[PTL-1::mNeonGreen]); vxEx1216[Pmec-17::ptl-1 sense and antisense CDS + Punc-122::RFP]*

JPS1823 *vxIs824[prab-3::ND18ApoE4::UNC54UTR, pmyo-2::mCherry::UNC54UTR]; ptl-1(syb8686 syb8597 pg73[LoxP::PTL-1::mNeonGreen::LoxP) III; hrtSi99[Pmec-17::Cre]*

JPS1824 *vxIs824[prab-3::ND18ApoE4::UNC54UTR, pmyo-2::mCherry::UNC54UTR]; ptl-1(syb8686 syb8597 pg73[LoxP::PTL-1::mNeonGreen::LoxP) III; hrtSi99[Pmec-17::Cre]*

469 **Generation of strains**

470 Presence of the 1933 bp deletion in *ptl-1* allele *ok621* was confirmed by PCR using the following
471 primers (written in 5'-3' orientation):

Forward: CTGGAAATTTGTTGGGCAGT

Reverse: TGAACCGAAGCCTAAACCAG

472 We sought to independently confirm the effect of pan-neuronal APOE4 on egg laying as well as
473 to test other behaviors with new extrachromosomal transgenic strains that carry a new reporter
474 that minimized effects on multiple behaviors. We transformed wild-type N2 with 20 ng/μL of the
475 APOE4 plasmid pPS90 (Sae-Lee et al., 2020) along with 10 ng/μL of the pCFJ104 mCherry
476 body wall reporter (Frøkjaer-Jensen et al., 2008) to generate the new extrachromosomal strain
477 JPS1453. In parallel, we transformed the *ptl-1*(*ok621*) mutant strain RB809 with the same DNA
478 mixture yielding the APOE4;Δ*ptl-1* strain JPS1455. We also generated control strain JPS1451
479 that carries the mCherry reporter alone.

480

481 To visualize the HSN axons, we used the *Ptph-1::gfp* reporter in strain JPS1571. This strain was
482 crossed with JPS1451 and JPS1453 to yield the control and APOE4 strains JPS1666 and
483 JPS1667, respectively. JPS1666 was then crossed with RB809 to yield the *Ptph-1::gfp*;Δ*ptl-1*
484 strain JPS1664. JPS1667 was crossed with RB809 to yield APOE4;Δ*ptl-1*, from which two
485 independent isolates were obtained, JPS1778 and JPS1779, to partly control for genetic
486 background.

487 **Cell-specific gene knockdown**

488 To knock down *ptl-1* specifically in the touch receptor neurons (TRNs), we followed previous
489 methods by Esposito et al. (See Fig. 1 of Esposito et al., 2007). The *mec-17* promoter (1535 bp)
490 was fused with either sense or antisense of *ptl-1* coding region (820 bp) to generate separate
491 DNA fragments using the following primers (written in 5'-3' orientation):

A

Forward: GGCTTGAATAATCCCTATTATAGCC

Reverse: GAAATTACCTGAAATTTCGTGGGG

B

Forward: GAGAAAACGGCCAATTGACGC

Reverse: GGCTATAATAGGGATTATTCAAGCCGATCGAATCGTCTCACAACTG

C

Forward: GAGAAAACGGCCAATTGACGC

Reverse: CCCCACGAAATTTCAGGTAATTTCGATCGAATCGTCTCACAACTG

D

Forward: CGTCGCGCTAACAGTTCTAG

Reverse: CCAAAGGTTAACGCCAAATTTG

E

Forward: CGTCGCGCTAACAGTTCTAG

Reverse: CAAGTGAAAGCGTGGTCCGATC

492 Fragments D and E were mixed in equimolar amounts, along with a selectable RFP
493 coelomocyte marker (Addgene Plasmid #8938), to a final concentration of 80 ng/µL. This DNA
494 mix was transformed into the *ptl-1*::*mNeonGreen* strain GN655 (PTL-1::mNG; Krieg et al.,
495 2017). The resultant strain, JPS1456, expresses *ptl-1* dsRNA fragments in the TRNs. JPS1456
496 was crossed into JPS1500, which carries an integrated pan-neuronal APOE4 transgene, to yield
497 two independent APOE4;TRNs::*ptl-1* KD strains named JPS1581 and JPS1582.

498 **Cell-specific gene knockout**

499 To knock out *ptl-1* in the TRNs, we commissioned SUNY Biotech to generate the strain
500 PHX8686 which harbors *LoxP* sites flanking the *ptl-1* genetic locus in the strain GN655.
501 PHX8686 was crossed into MSB1167, a transgenic line in which Cre recombinase is expressed
502 under control of the *mec-17* promoter (Harterink et al., 2018). This yielded the TRNs::*ptl-1* KO
503 strain JPS1819. The presence of PTL-1::mNG in the TRNs was determined with epifluorescent

504 microscopy. Lastly, JPS1819 was crossed into JPS1500 to yield APOE4;TRNs::*ptl-1* KO, from
505 which two independent isolates were obtained which are JPS1823 and JPS1824, to partly
506 control for genetic background.

507 **Cell-specific ablation**

508 To genetically ablate the TRNs, we used the TRN-specific *mec-17* promoter to express *egl-1* in
509 an extrachromosomal array in strain JPS1828 (Wu et al., 2025). This strain was crossed into
510 JPS1500, a strain carrying an integrated pan-neuronal APOE4 transgene and a *Punc-122*::*gfp*
511 reporter, to yield strain JPS1839. Additionally, we crossed JPS1500 into TU253, which carries
512 *mec-4* null mutation (O'Hagan et al., 2004), to yield strain APOE4;*mec-4* JPS1709.

513 **Sterilization**

514 To inspect HSN neuron health without confounding effects of the bagging phenotype, worms
515 were sterilized as previously described (Mitchell et al., 1979). In brief, seeded plates were
516 pretreated with 600 mL of 0.8 mM 5'-fluorodeoxyuridine (FUdR; FUdR plates). Mid- to late-stage
517 L4 stage worms were transferred onto FUDR plates and moved to fresh FUdR plates every 1-2
518 days as needed.

519 **Behavioral assays**

520 Behavioral assays were performed on either 60 mm (medium) or 35 mm (small) NGM plates,
521 seeded or not with OP50 bacteria as described per assay. All assays were performed at room
522 temperature (20° C) unless stated otherwise. Assays began with day 1 adults (D1), 24 hours
523 after initial incubation on FUDR plates (if applicable), until a significant difference between
524 control and APOE4 worms was observed. Completely immobile worms or those which escaped
525 from the side of the plate were omitted from assays and final quantifications.

526 **Gentle touch**

527 Methods adapted from Chalfie and Sulston (1981). In brief, 20-30 worms were moved to
528 medium NGM-OP50 plates. To test gentle touch sensitivity, an eyelash hair, affixed by its shaft
529 to a pipette tip, was used to deliver mechanical stimuli to worms. Gentle strokes were applied to
530 the posterior and anterior of the animal. Six paired anterior and posterior stimuli were applied,

531 with an interstimulus interval of approximately 1.5 seconds to avoid habituation. Gentle touch
532 sensitivity was quantified per worm as the fraction of responses to stimuli out of 12.

533 **Harsh touch**

534 Methods adapted from Li et al. (2011). In brief, 20-30 worms were moved to medium NGM-
535 OP50 plates. To test harsh gentle touch sensitivity, a single prod was delivered to the mid-body
536 using a platinum pick. Five technical replicates were performed per worm per strain. Harsh
537 touch sensitivity was quantified per replicate as the proportion of responsive worms.

538 **Pharyngeal pumping**

539 Methods adapted from Avery and Shtonda (2003). In brief, 30-40 worms were first moved to
540 medium NGM-OP50 plates. Worms were allowed to roam for at least 30 minutes. Individual
541 animals were then tracked for 20 seconds and pharyngeal bulb contractions were manually
542 tallied with a handheld click counter. Pumping rate was quantified per worm as pumps per
543 minute.

544 **Bagging**

545 Methods adapted from Sae-Lee et al. (2020). In brief, at least 30-40 L4-stage worms were
546 moved to medium NGM-OP50 plates. Worms were scored daily for the internal hatching or
547 “bagging” phenotype based on presence or absence of several late-stage eggs and/or hatched
548 larvae within the uterus; this is often accompanied by general lethargy plus distension of the
549 worm midbody as previously described (Trent et al., 1983). Bagging worms were tallied and
550 discarded while non-bagging worms were transferred to a fresh medium NGM-OP50 plate.
551 Worms were scored in this fashion from D1 to D4 of adulthood. Bagging incidence was
552 quantified per replicate as the cumulative percentage of bagging worms summed across D1-4
553 out of the original total.

554 **Long-term locomotion**

555 Methods adapted from Nordquist et al. (2018). Single worms were moved to the center of a
556 small NGM plate uniformly seeded with OP50 such that the lawn covered the entirety of the
557 NGM surface. Animals were incubated on these assay plates overnight at 22°C. Groups of at

558 least 8 worms per genotype were tested on two separate days as also described by Nordquist
559 et al. After 18 hours, the worms were removed from their plates and a transparent grid guide
560 was used to determine the number of ~5 mm^2 regions (32 in total) traversed on the assay plate.
561 Regions encompassing parts of the NGM which split or pulled away from the plastic of the plate
562 were omitted from the total. Long-term locomotion was quantified per worm as the proportion of
563 traversed regions on the assay plate out of the total.

564 **Short-term locomotion**

565 Methods adapted from Topalidou et al. (2017). In brief, 8-10 worms were moved to the center of
566 a medium NGM-OP50 plate which was uniformly seeded such that the bacterial lawn extended
567 across the entire medium surface. After 10 minutes, worms were removed and their final
568 positions marked on the plate. Groups of least 15 worms per genotype were tested on two
569 separate days as previously described (Nordquist et al., 2018). The distance which they had
570 radially dispersed was recorded. Short-term locomotion was quantified per worm as the
571 distance (cm) from the center to final positions.

572 **Swim-to-crawl gait transition**

573 Methods adapted from Vidal-Gadea et al. (2011). Before testing, 25-40 worms were moved to a
574 medium NGM plate and allowed to roam for ~15 minutes so excess OP50 could be removed.
575 Meanwhile, assay plates were prepared by first drawing a 0.5 cm radius border on the plastic
576 behind its center. Next, 10 uL of liquid NGM was pipetted to the very center of the assay plate
577 surface. Worms were then picked to the center of the puddle on the assay plate and a 15-
578 minute timer was started. As the puddle dried, swimming worms began to escape to the solid
579 surface, transition to a crawling gait, and disperse away from the puddle. Gait transition was
580 quantified per replicate as the proportion of worms which escaped and crawled past the 0.5 cm
581 border in under 15 minutes.

582 **Microscopy**

583 Epifluorescent microscopy was performed on an Olympus IX51 inverted microscope with an
584 Olympus UPlanFL N 40X/0.75 NA objective and X-Cite FIRE LED Illuminator (Excelitas

585 Technologies Corp.). Images were captured using a Retiga 2000R CCD camera (QImaging)
586 and QCapture Pro 6.0 software.

587 Worms were sterilized with FUDR as described above to prevent internally hatching
588 larvae that may affect HSN morphology. Worms were then mounted on 2% agarose pads and
589 immobilized using 50 mM sodium azide. All imaging per pad took place within 30 minutes of
590 mounting.

591 The same fluorescence intensity settings were used to image all HSN soma and
592 proximal axons via a GFP reporter. Importantly, imaging was restricted to worms which lay in a
593 strictly lateral orientation (i.e., on the right or left side with minimal twisting about the long axis of
594 the animal). This ensured both the soma and proximal axon of a given HSN neuron were in
595 approximately the same focal plane. We determined the orientation of mounted worms using the
596 fluorescent co-injection marker expressed in the strains which were imaged. This marker labels
597 body wall and vulval musculature with mCherry, visualizable in the red channel. In single focal
598 planes, the labeled vulval muscles either appear as an x-shape from a ventral viewpoint or a v-
599 shape if the animal laid directly on its right or left side as described above (See also Fig. 1 of
600 Collins and Koelle, 2020). Incidentally, the HSN GFP reporter also labels the VC4 and VC5
601 motor neurons, which are visible in the “v-shape” focal plane. These guides helped restrict our
602 microscopy to animals in the desired orientation described above.

603 After imaging, morphometrics of HSN soma and proximal axons were calculated in
604 ImageJ (Schneider et al., 2012). Positions of HSN soma were determined by measuring the
605 lengths of the vector from the soma to the ventral nerve cord (HSN-VNC, met at a
606 perpendicular) and the vector to the vulval area in between VCs4,5 (HSN-vulva). These
607 measurements were also collapsed into a single metric as previously described (Asakura et al.,
608 2007). This metric, represented by θ, is the angle in degrees between the HSN-vulva
609 (hypotenuse) and HSN-VNC (adjacent) vectors (i.e., arccosine of their ratio).

610 HSN proximal axon lengths were calculated with the NeuronJ plugin for ImageJ using
611 default settings (Meijering et al., 2004). Traces were made by following the proximal axon from

612 anterior face of the HSN soma to the point at which the axon exits the focal plane ventrally in
613 the vulval area. Ectopic sprouts from the soma or proximal axon were excluded from tracing. In
614 the rare (<5% frequency) cases where ectopic sprouts were present on the proximal axon, the
615 shortest ventral and vulval-directed course was traced for all strains imaged.

616 To capture images of PTL-1::mNG strains, an increased exposure time and intensity
617 setting were required compared to HSN GFP reporter strains. Because some TRN processes
618 span nearly the entire animal length, we chose to focus on soma to quantify PTL-1::mNG signal
619 in TRNs::*ptl-1* KD strain JPS1456 and control strain GN655 (See Fig. 3). Depending on animal
620 orientation, bilateral TRN soma were identifiable based on the naturally asymmetric positioning
621 of the AVM and PVM class neurons (Arnold et al., 2020). The VCs4,5 neurons were almost
622 always visualizable regardless of orientation, making them ideal for internal controls.
623 Fluorescence intensity was quantified in ImageJ in day 1 adults.

624 In the TRNs::*ptl-1* KO strain JPS1819, *LoxP*-flanked *ptl-1* is presumably excised by Cre
625 recombinase whose expression is driven by the *mec-17* promoter (Harterink et al., 2018).
626 Although *mec-17* expression begins embryonically in ALM and PLM class TRNs (Roux et al.,
627 2023), residual PTL-1::mNG is still present by at least L4 stage of development; PTL-1::mNG is
628 qualitatively fainter in those cells compared to like-aged control animals (GN655 strain). Thus,
629 selection for animals with lacking PTL-1::mNG in PLM neurons was conducted in at least day 1
630 adults to avoid ambiguity. This selection strategy was also employed in the TRNs::EGL-1 strain
631 JPS1828 to identify animals with genetically ablated TRNs.

632 **Western blotting**

633 Worms were washed twice with 5% sucrose and twice with 50 mM NaCl before being
634 flash frozen with 5µl glass beads.

635 For worm lysis, 2% PMSF was added to 2x Laemmli buffer. This buffer was then added
636 to the frozen samples to achieve a 1x concentration. Finally, 5% β-mercaptoethanol
637 (BME) was added to the samples before bead beating, which was performed for 30
638 seconds. Samples were spun down through centrifugation for 2 minutes at 15,000 g.

639 The samples were then boiled at 95℃ for 5 minutes. An additional 2-minute
640 centrifugation was performed to clear debris prior to measuring protein concentration
641 with Qubit Protein Assay Kit (Thermo Scientific, #Q33211).
642 20 µg of protein per sample was loaded on Invitrogen™ NuPAGE™ Bis-Tris Mini
643 Protein Gels (4–12%, 1.0–1.5 mm, Invitrogen, #NP0335) and separated at 80-120 V in
644 1X MES SDS running buffer. Proteins were transferred onto a PVDF membrane
645 (Thermo Scientific, #88518) at 30V for 1 hour.
646 Membranes were blocked in 1X TBS Tween 20 Buffer (Thermo Scientific, #28360)
647 containing 5% milk. Flag tag and actin were probed with primary antibodies: Monoclonal
648 ANTI-FLAG® M2 antibody produced in mouse (1:2,000, Sigma-Aldrich, #F3165) and
649 Anti-Actin Mouse Monoclonal Antibody [clone: C4] (1:500, MP Biomedicals,
650 #08691001), respectively. A secondary antibody, Goat anti-Mouse IgG (H+L)
651 Superclonal™ Secondary Antibody, Alexa Fluor™ 488 (1:4,000, Invitrogen, #A28175)
652 was used after flag and actin probing. Finally, an Amersham™ Typhoon™ RGB was
653 utilized for visualization.
654 **Statistical analysis**
655 All data are presented as the mean ± SEM. Plotted data points represent individuals or
656 the average across a single replicate as indicated in figures. Total sample size (N) is indicated
657 in figure legends. Behavioral assays and microscopy scoring were performed blind to genotype.
658 χ^2 tests of independence were performed for statistical comparisons of gait transition (escaped
659 vs. not escaped), bagging (yes vs. no), and HSN axon scoring (normal vs. abnormal). One-
660 tailed Student t-tests were performed for statistical comparisons of touch, pumping, locomotion
661 behaviors, HSN axon length, HSN soma position, and fluorescence intensity.
662
663

664 **Acknowledgements**

665 We would like to thank Drs. Miriam B. Goodman and Michael Krieg for sharing strains GN655
666 and MSB1167, respectively, and SUNY Biotech for engineering PHX8686. Some strains were
667 also provided by the *Caenorhabditis* Genetics Center, which is funded by the NIH Center for
668 Research Resources. We also thank Chelsea Webber for constructive feedback on manuscript
669 drafts.

670

671 **Footnotes**

672 **Author contributions**

673 Conceptualization: J.T.P., E.A.C.; Methodology: E.A.C., Z.W., J.T.P.; Investigation: E.A.C.,
674 Z.W., B.M.B., E.S.-C., J.T.P.; Writing – original draft: E.A.C., J.T.P.; Writing – review and
675 editing: E.A.C., Z.W., E.S.-C., J.T.P.; Funding acquisition: E.S.-C., J.T.P.

676 **Funding**

677 This work was funded in part by the NIH (R01GM122463, RF1AG057355, R21OD032463 -
678 J.T.P.) Waggoner Fellowship for Alcohol Research (J.T.P.), David and Ellen Berman
679 Fellowships for Huntington's Research (J.T.P.), George and Karen Casey (J.T.P.), Pine Family
680 Foundation (J.T.P.), CNS Catalyst Grant (J.T.P. and E.S.C.), National Institutes of Health (NIH)
681 NIGMS (R35GM138340) (E.S.C.), Welch Foundation (F-2133-20230405) (E.S.C.), and F.M.
682 Jones and H.L. Bruce Graduate Fellowship (Z.W.).

683 **Data availability**

684 All relevant data can be found either within the article or in its supplementary information
685 section. Raw data is available upon request.

686 **Competing interests**

687 The authors declare no competing or financial interests.

688
689
690
691

692

693 **Figure Legends**

694

695 **Figure 1. *ptl-1* is required for widespread, progressive neuronal dysfunction induced by APOE4.**

696 (A left) Timeline from egg lay to the adult age of onset at which defective or abnormal performance in

697 APOE4 versus control animals are first detected.

698 (A right) Endogenous *ptl-1* locus with all known isoforms and the portion deleted in the *ok621* allele as

699 indicated below.

700 (B-H) Results of behavioral assays, used to proxy neuronal dysfunction, which are arranged by the adult

701 age of onset for APOE4-induced defective or abnormal performance.

702 (B-E) D1 adult onset. (B) Subtle defect in gentle touch sensitivity which is fully suppressed by *ptl-1*

703 deletion. N=47 for control, N=30 for Δ*ptl-1*, N=33 for APOE4, and N=35 for APOE4;Δ*ptl-1*. (C) Subtle

704 defect in pharyngeal pumping which is fully suppressed by *ptl-1* deletion. N=94 for control, N=37 for Δ*ptl-*

705 *1*, N=61 for APOE4, and N=91 for APOE4;Δ*ptl-1*. (D) Severe defect in swim-to-crawl gait transition which

706 is partially suppressed by *ptl-1* deletion. N=164 control, N=136 for Δ*ptl-1*, N=162 for APOE4, N=165 for

707 APOE4;Δ*ptl-1*. (E) Subtle defect in short-term locomotion which is not suppressed by *ptl-1* deletion. N=47

708 for control, N=38 for Δ*ptl-1*, N=44 for APOE4, and N=44 for APOE4;Δ*ptl-1*).

709 (F) D2 adult onset. Subtle defect in long-term locomotion which is not suppressed by *ptl-1* deletion. N=31

710 control, N=32 for Δ*ptl-1*, N=28 for APOE4, and N=29 for APOE4;Δ*ptl-1*.

711 (G,H) D3 adult onset. (G) Severe egg laying defect which is partially suppressed by *ptl-1* deletion. N=196

712 for control, N=134 for Δ*ptl-1*, N=214 for APOE4, N=243 for APOE4;Δ*ptl-1*. (H) Subtle, abnormal increase

713 in harsh touch sensitivity. N=25 for control, N=17 for Δ*ptl-1*, N=26 for APOE4, and N=31 for APOE4;Δ*ptl-*

714 *1*.

715 All data are represented as mean ± SEM. N is the total sample size representing all animals across

716 replicates. Statistical comparisons were made using χ^2 tests of independence for D,G and Student's t-test

717 for B,C,E,F,G. *: $p<0.05$; **: $p<0.01$; ***: $p<0.001$.

718

719 **Figure 2. *ptl-1* is required for APOE4-induced HSN axon degeneration.**

720 (A) Cartoon of the worm midbody, centered about the vulva area, depicting: the HSN proximal
721 axon, the VC4,5 neurons, vulval musculature, and ventral nerve cord (VNC).
722 (B) Representative live images of normal (1,2) and abnormal (3-10) HSN proximal axons
723 visualized with GFP. Proximal axon segments are marked by i. and ii (with exception to image
724 2, where segment identity is less certain). The vulva area is also marked with a white arrowhead
725 for anatomical reference. All scale bars are 20 μm.
726 (C,D) Percentage of animals with abnormal HSN proximal axons in D1 and D3 adults. The
727 baseline incidence of abnormal axons in control was similar between D1 and D3.
728 (C) D1 adults. All other groups show non-significant, but slightly increased incidence of
729 abnormal axons compared to control. N=37 for control, N=59 Δ*ptl-1*, N=51 for APOE4, N=22 for
730 APOE4;Δ*ptl-1* (left), and N=37 for APOE4;Δ*ptl-1* (right).
731 (D) The incidence of abnormal axons appears to correlate with defective egg laying behavior
732 (See Fig. 1G) in D3 adults. N=101 for control, N=78 for Δ*ptl-1*, N=91 for APOE4, N=79 for
733 APOE4;Δ*ptl-1* (left), and N=86 for APOE4;Δ*ptl-1* (right).
734 (E,F) Quantification of HSN proximal axon lengths in D1 and D3 adults. The baseline axon
735 length in control was similar between D1 and D3.
736 (E) D1 adults. Axon length was similar across all groups. N=15 for control, N=13 Δ*ptl-1*, N=20
737 for APOE4, N=6 for APOE4;Δ*ptl-1* (left), and N=10 for APOE4;Δ*ptl-1* (right).
738 (D) D3 adults. Axon length appears to correlate with the incidence of abnormal axons shown in
739 (C) and defective egg laying behavior (See Fig. 1G). N=79 for control, N=66 for Δ*ptl-1*, N=72 for
740 APOE4, N=54 for APOE4;Δ*ptl-1* (left), and N=66 for APOE4;Δ*ptl-1* (right).
741 All data are represented as mean ± SEM. N is the total sample size representing all animals
742 across replicates. Statistical comparisons were made using χ^2 tests of independence for C and
743 D and Student's t-test for (E) and (F). *: $p<0.05$; **: $p<0.01$; ***: $p<0.001$.
744
745 **Figure 2. *ptl-1* is required for APOE4-induced HSN axon degeneration.**

746 (A) Cartoon of the worm midbody, centered about the vulva area, depicting: the HSN proximal
747 axon, the VC4,5 neurons, vulval musculature, and ventral nerve cord (VNC).
748 (B) Representative live images of normal (1,2) and abnormal (3-10) HSN proximal axons
749 visualized with GFP. Proximal axon segments are marked by i. and ii (with exception to image
750 2, where segment identity is less certain). The vulva area is also marked with a white arrowhead
751 for anatomical reference. All scale bars are 20 μm.
752 (C,D) Percentage of animals with abnormal HSN proximal axons in D1 and D3 adults. The
753 baseline incidence of abnormal axons in control was similar between D1 and D3.
754 (C) D1 adults. All other groups show non-significant, but slightly increased incidence of
755 abnormal axons compared to control. N=37 for control, N=59 Δ*ptl-1*, N=51 for APOE4, N=22 for
756 APOE4;Δ*ptl-1* (left), and N=37 for APOE4;Δ*ptl-1* (right).
757 (D) The incidence of abnormal axons appears to correlate with defective egg laying behavior
758 (See Fig. 1G) in D3 adults. N=101 for control, N=78 for Δ*ptl-1*, N=91 for APOE4, N=79 for
759 APOE4;Δ*ptl-1* (left), and N=86 for APOE4;Δ*ptl-1* (right).
760 (E,F) Quantification of HSN proximal axon lengths in D1 and D3 adults. The baseline axon
761 length in control was similar between D1 and D3.
762 (E) D1 adults. Axon length was similar across all groups. N=15 for control, N=13 Δ*ptl-1*, N=20
763 for APOE4, N=6 for APOE4;Δ*ptl-1* (left), and N=10 for APOE4;Δ*ptl-1* (right).
764 (D) D3 adults. Axon length appears to correlate with the incidence of abnormal axons shown in
765 (C) and defective egg laying behavior (See Fig. 1G). N=79 for control, N=66 for Δ*ptl-1*, N=72 for
766 APOE4, N=54 for APOE4;Δ*ptl-1* (left), and N=66 for APOE4;Δ*ptl-1* (right).
767 All data are represented as mean ± SEM. N is the total sample size representing all animals
768 across replicates. Statistical comparisons were made using χ^2 tests of independence for C and
769 D and Student's t-test for (E) and (F). *: $p<0.05$; **: $p<0.01$; ***: $p<0.001$.
770
771 **Figure 3. Targeted genetic ablation, but not abolished function, of the TRNs protects HSN**
772 **against APOE4-induced dysfunction.**

773 (A1) Egg-laying behavior across groups. Genetic ablation of the TRNs partially suppressed egg-
774 laying defects in APOE4 animals as with the *ptl-1* deletion (See Fig. 1G). N=104 for control,
775 N=171 for TRNs::EGL-1, N=525 for APOE4, and N=190 for APOE4;TRNs::EGL-1.
776 (A2 top) Cartoon depicting the head and tail areas wherein the nerve ring and PLM neuron,
777 respectively, are located.
778 (A2 bottom) Representative live images of nerve ring (arrowhead) and PLM neuron (within
779 dashed circle if present; marked with asterisk if absent) visualized with PTL-1::mNG in control
780 and TRNs::EGL-1 animals. Dashed borders indicate the worm body outline. All scale bars are
781 20 μm.
782 (B) Egg-laying behavior across groups. In contrast to genetic ablation, abolishing TRN function
783 did not suppress egg laying defects. N=104 for control, N=123 for *mec-4*(*lf*), N=525 for APOE4,
784 and N=101 for APOE4;*mec-4*(*lf*) (left), and N=125 for APOE4;*mec-4*(*lf*) (right).
785 All data are represented as mean ± SEM. N is the total sample size representing all animals
786 across replicates. All statistical comparisons were made using χ^2 tests of independence. control
787 and APOE4 data are re-plotted in (A1) and (B). *: $p<0.05$; **: $p<0.01$; ***: $p<0.001$.
788
789 **Figure 4. Targeted depletion of PTL-1 in the TRNs protects HSN against APOE4-induced**
790 **dysfunction.**
791 (A1) Egg-laying behavior across groups. N=104 for control, N=180 for TRNs::*ptl-1* KD, N=525
792 for APOE4, N=171 for APOE4;TRNs:: *ptl-1* KD (Left), and N=108 for APOE4;TRNs:: *ptl-1* KD
793 (Right).
794 (A2) Quantification of *ptl-1* knockdown in the targeted TRNs and non-targeted VCs4,5 neurons
795 between control and TRNs::*ptl-1* KD animals using PTL-1::mNG fluorescence intensity in the
796 soma.
797 (B1) Egg-laying behavior across groups. N=104 for control, N=348 for TRNs::*ptl-1* KO, N=525
798 for APOE4, N=423 for APOE4;TRNs:: *ptl-1* KO (*Left*), and N=519 for APOE4;TRNs:: *ptl-1* KO
799 (Right).

800 (B2) Representative live images of nerve ring (arrowhead) and PLM neuron (within dashed
801 circle if present; area marked with asterisk if absent) visualized with PTL-1::mNG in control and
802 TRNs::*ptl-1* KO animals. Dashed borders indicate the worm body outline. All scale bars are 20
803 µm.
804 All data are represented as mean ± SEM. N is the total sample size representing all animals
805 across replicates. Statistical comparisons were made using χ^2 tests of independence for A1,B1
806 and Student's t-test for A2. Control and APOE4 data are re-plotted in (A1) and (B1). *: $p<0.05$;
807 **: $p<0.01$; ***: $p<0.001$.
808

809 **References**

810 ▪ Andrews-Zwilling, Y., Bien-Ly, N., Xu, Q., Li, G., Bernardo, A., Yoon, S. Y., Zwilling, D., Yan,
811 T. X., Chen, L., and Huang, Y. (2010). Apolipoprotein E4 causes age- and Tau-dependent
812 impairment of GABAergic interneurons, leading to learning and memory deficits in mice. *The*
813 *Journal of neuroscience : the official journal of the Society for Neuroscience*, *30*(41), 13707–
814 13717. https://doi.org/10.1523/JNEUROSCI.4040-10.2010
815 ▪ Aquino Nunez, W., Combs, B., Gamblin, T. C., and Ackley, B. D. (2022). Age-dependent
816 accumulation of tau aggregation in *Caenorhabditis elegans*. *Frontiers in aging*, *3*, 928574.
817 https://doi.org/10.3389/fragi.2022.928574
818 ▪ Arnold, M. L., Cooper, J., Grant, B. D., & Driscoll, M. (2020). Quantitative Approaches for
819 Scoring in vivo Neuronal Aggregate and Organelle Extrusion in Large Exopher Vesicles in
820 C. elegans. *Journal of visualized experiments : JoVE*, (163), 10.3791/61368.
821 https://doi.org/10.3791/61368
822 ▪ Asakura, T., Ogura, K., and Goshima, Y. (2007). UNC-6 expression by the vulval precursor
823 cells of Caenorhabditis elegans is required for the complex axon guidance of the HSN
824 neurons. *Developmental biology*, *304*(2), 800–810.
825 https://doi.org/10.1016/j.ydbio.2007.01.028
826 ▪ Avery, L., and Shtonda, B. B. (2003). Food transport in the C. elegans pharynx. *The Journal*
827 *of experimental biology*, *206*(Pt 14), 2441–2457. https://doi.org/10.1242/jeb.00433
828 ▪ Avery, L., and You, Y. J. (2012). C. elegans feeding. *WormBook : the online review of C.*
829 *elegans biology*, 1–23. https://doi.org/10.1895/wormbook.1.150.1
830 ▪ Baskoylu, S. N., Yersak, J., O'Hern, P., Grosser, S., Simon, J., Kim, S., Schuch, K.,
831 Dimitriadi, M., Yanagi, K. S., Lins, J., and Hart, A. C. (2018). Single copy/knock-in models of
832 ALS SOD1 in C. elegans suggest loss and gain of function have different contributions to

833 cholinergic and glutamatergic neurodegeneration. *PLoS genetics*, *14*(10), e1007682.
834 https://doi.org/10.1371/journal.pgen.1007682
835 ▪ Benbow, S. J., Strovas, T. J., Darvas, M., Saxton, A., and Kraemer, B. C. (2020). Synergistic
836 toxicity between tau and amyloid drives neuronal dysfunction and neurodegeneration in
837 transgenic C. elegans. *Human molecular genetics*, *29*(3), 495–505.
838 https://doi.org/10.1093/hmg/ddz319
839 ▪ Benzing, W. C., and Mufson, E. J. (1995). Apolipoprotein E immunoreactivity within
840 neurofibrillary tangles: relationship to Tau and PHF in Alzheimer's disease. *Experimental*
841 *neurology*, *132*(2), 162–171. https://doi.org/10.1016/0014-4886(95)90021-7
842 ▪ Bookheimer, S. Y., Strojwas, M. H., Cohen, M. S., Saunders, A. M., Pericak-Vance, M. A.,
843 Mazziotta, J. C., and Small, G. W. (2000). Patterns of brain activation in people at risk for
844 Alzheimer's disease. *The New England journal of medicine*, *343*(7), 450–456.
845 https://doi.org/10.1056/NEJM200008173430701
846 ▪ Braak, H., and Braak, E. (1991). Neuropathological stageing of Alzheimer-related changes.
847 *Acta neuropathologica*, *82*(4), 239–259. https://doi.org/10.1007/BF00308809
848 ▪ Braak, H., & Del Tredici, K. (2011). Alzheimer's pathogenesis: is there neuron-to-neuron
849 propagation?. *Acta neuropathologica*, *121*(5), 589–595. https://doi.org/10.1007/s00401-011-
850 0825-z
851 ▪ Brenner S. (1974). The genetics of Caenorhabditis elegans. *Genetics*, *77*(1), 71–94.
852 https://doi.org/10.1093/genetics/77.1.71
853 ▪ Brecht, W. J., Harris, F. M., Chang, S., Tesseur, I., Yu, G. Q., Xu, Q., Dee Fish, J., Wyss-
854 Coray, T., Buttini, M., Mucke, L., Mahley, R. W., and Huang, Y. (2004). Neuron-specific
855 apolipoprotein e4 proteolysis is associated with increased tau phosphorylation in brains of
856 transgenic mice. *The Journal of neuroscience : the official journal of the Society for*
857 *Neuroscience*, *24*(10), 2527–2534. https://doi.org/10.1523/JNEUROSCI.4315-03.2004
858 ▪ Butner, K. A., and Kirschner, M. W. (1991). Tau protein binds to microtubules through a
859 flexible array of distributed weak sites. *The Journal of cell biology*, *115*(3), 717–730.
860 https://doi.org/10.1083/jcb.115.3.717
861 ▪ Chalfie, M., and Sulston, J. (1981). Developmental genetics of the mechanosensory
862 neurons of Caenorhabditis elegans. *Developmental biology*, *82*(2), 358–370.
863 https://doi.org/10.1016/0012-1606(81)90459-0
864 ▪ Chalfie, M., and Thomson, J. N. (1979). Organization of neuronal microtubules in the
865 nematode Caenorhabditis elegans. *The Journal of cell biology*, *82*(1), 278–289.
866 https://doi.org/10.1083/jcb.82.1.278

867 ▪ Chalfie, M., and Thomson, J. N. (1982). Structural and functional diversity in the neuronal
868 microtubules of Caenorhabditis elegans. *The Journal of cell biology*, *93*(1), 15–23.
869 https://doi.org/10.1083/jcb.93.1.15
870 ▪ Chalfie, M., Sulston, J. E., White, J. G., Southgate, E., Thomson, J. N., and Brenner, S.
871 (1985). The neural circuit for touch sensitivity in Caenorhabditis elegans. *The Journal of*
872 *neuroscience : the official journal of the Society for Neuroscience*, *5*(4), 956–964.
873 https://doi.org/10.1523/JNEUROSCI.05-04-00956.1985
874 ▪ Chang, A. J., Chronis, N., Karow, D. S., Marletta, M. A., and Bargmann, C. I. (2006). A
875 distributed chemosensory circuit for oxygen preference in C. elegans. *PLoS biology*, *4*(9),
876 e274. https://doi.org/10.1371/journal.pbio.0040274
877 ▪ Clavaguera, F., Bolmont, T., Crowther, R. A., Abramowski, D., Frank, S., Probst, A., Fraser,
878 G., Stalder, A. K., Beibel, M., Staufenbiel, M., Jucker, M., Goedert, M., and Tolnay, M.
879 (2009). Transmission and spreading of tauopathy in transgenic mouse brain. *Nature cell*
880 *biology*, *11*(7), 909–913. https://doi.org/10.1038/ncb1901
881 ▪ Coakley, S., Ritchie, F. K., Galbraith, K. M., and Hilliard, M. A. (2020). Epidermal control of
882 axonal attachment via β-spectrin and the GTPase-activating protein TBC-10 prevents
883 axonal degeneration. *Nature communications*, *11*(1), 133. https://doi.org/10.1038/s41467-
884 019-13795-x
885 ▪ Cornblath, E. J., Li, H. L., Changolkar, L., Zhang, B., Brown, H. J., Gathagan, R. J., Olufemi,
886 M. F., Trojanowski, J. Q., Bassett, D. S., Lee, V. M. Y., and Henderson, M. X. (2021).
887 Computational modeling of tau pathology spread reveals patterns of regional vulnerability
888 and the impact of a genetic risk factor. *Science advances*, *7*(24), eabg6677.
889 https://doi.org/10.1126/sciadv.abg6677
890 ▪ Crespo-Biel, N., Theunis, C., Borghgraef, P., Lechat, B., Devijver, H., Maurin, H., and Van
891 Leuven, F. (2014). Phosphorylation of protein Tau by GSK3β prolongs survival of bigenic
892 Tau.P301L×GSK3β mice by delaying brainstem tauopathy. *Neurobiology of disease*, *67*,
893 119–132. https://doi.org/10.1016/j.nbd.2014.03.016
894 ▪ Daigle, I., and Li, C. (1993). apl-1, a Caenorhabditis elegans gene encoding a protein
895 related to the human beta-amyloid protein precursor. *Proceedings of the National Academy*
896 *of Sciences of the United States of America*, *90*(24), 12045–12049.
897 https://doi.org/10.1073/pnas.90.24.12045
898 ▪ Davis, A. A., Inman, C. E., Wargel, Z. M., Dube, U., Freeberg, B. M., Galluppi, A., Haines, J.
899 N., Dhavale, D. D., Miller, R., Choudhury, F. A., Sullivan, P. M., Cruchaga, C., Perlmutter, J.
900 S., Ulrich, J. D., Benitez, B. A., Kotzbauer, P. T., and Holtzman, D. M. (2020). *APOE*
901 genotype regulates pathology and disease progression in synucleinopathy. *Science*
902 *translational medicine*, *12*(529), eaay3069. https://doi.org/10.1126/scitranslmed.aay3069

903 ▪ de Calignon, A., Polydoro, M., Suárez-Calvet, M., William, C., Adamowicz, D. H., Kopeikina,
904 K. J., Pitstick, R., Sahara, N., Ashe, K. H., Carlson, G. A., Spires-Jones, T. L., and Hyman,
905 B. T. (2012). Propagation of tau pathology in a model of early Alzheimer's disease. *Neuron*,
906 *73*(4), 685–697. https://doi.org/10.1016/j.neuron.2011.11.033
907 ▪ DeVos, S. L., Miller, R. L., Schoch, K. M., Holmes, B. B., Kebodeaux, C. S., Wegener, A. J.,
908 Chen, G., Shen, T., Tran, H., Nichols, B., Zanardi, T. A., Kordasiewicz, H. B., Swayze, E. E.,
909 Bennett, C. F., Diamond, M. I., and Miller, T. M. (2017). Tau reduction prevents neuronal
910 loss and reverses pathological tau deposition and seeding in mice with tauopathy. *Science*
911 *translational medicine*, *9*(374), eaag0481. https://doi.org/10.1126/scitranslmed.aag0481
912 ▪ Eichel, K., Uenaka, T., Belapurkar, V., Lu, R., Cheng, S., Pak, J. S., Taylor, C. A., Südhof, T.
913 C., Malenka, R., Wernig, M., Özkan, E., Perrais, D., and Shen, K. (2022). Endocytosis in the
914 axon initial segment maintains neuronal polarity. *Nature*, *609*(7925), 128–135.
915 https://doi.org/10.1038/s41586-022-05074-5
916 ▪ Esposito, G., Di Schiavi, E., Bergamasco, C., and Bazzicalupo, P. (2007). Efficient and cell
917 specific knock-down of gene function in targeted C. elegans neurons. *Gene*, *395*(1-2), 170–
918 176. https://doi.org/10.1016/j.gene.2007.03.002
919 ▪ Faber, P. W., Alter, J. R., MacDonald, M. E., and Hart, A. C. (1999). Polyglutamine-
920 mediated dysfunction and apoptotic death of a Caenorhabditis elegans sensory neuron.
921 *Proceedings of the National Academy of Sciences of the United States of America*, *96*(1),
922 179–184. https://doi.org/10.1073/pnas.96.1.179
923 ▪ Fatouros, C., Pir, G. J., Biernat, J., Koushika, S. P., Mandelkow, E., Mandelkow, E. M.,
924 Schmidt, E., and Baumeister, R. (2012). Inhibition of tau aggregation in a novel
925 Caenorhabditis elegans model of tauopathy mitigates proteotoxicity. *Human molecular*
926 *genetics*, *21*(16), 3587–3603. https://doi.org/10.1093/hmg/dds190
927 ▪ Fiford, C. M., Ridgway, G. R., Cash, D. M., Modat, M., Nicholas, J., Manning, E. N., Malone,
928 I. B., Biessels, G. J., Ourselin, S., Carmichael, O. T., Cardoso, M. J., Barnes, J., and
929 Alzheimer's Disease Neuroimaging Initiative (2018). Patterns of progressive atrophy vary
930 with age in Alzheimer's disease patients. *Neurobiology of aging*, *63*, 22–32.
931 https://doi.org/10.1016/j.neurobiolaging.2017.11.002
932 ▪ Flavell, S. W., Raizen, D. M., and You, Y. J. (2020). Behavioral States. *Genetics*, *216*(2),
933 315–332. https://doi.org/10.1534/genetics.120.303539
934 ▪ Fortea, J., Pegueroles, J., Alcolea, D., Belbin, O., Dols-Icardo, O., Vaqué-Alcázar, L., Videla,
935 L., Gispert, J. D., Suárez-Calvet, M., Johnson, S. C., Sperling, R., Bejanin, A., Lleó, A., and
936 Montal, V. (2024). APOE4 homozygozity represents a distinct genetic form of Alzheimer's
937 disease. *Nature medicine*, *30*(5), 1284–1291. https://doi.org/10.1038/s41591-024-02931-w

938 ▪ Friedhoff, P., Schneider, A., Mandelkow, E. M., and Mandelkow, E. (1998). Rapid assembly
939 of Alzheimer-like paired helical filaments from microtubule-associated protein tau monitored
940 by fluorescence in solution. *Biochemistry*, *37*(28), 10223–10230.
941 https://doi.org/10.1021/bi980537d
942 ▪ Friedhoff, P., von Bergen, M., Mandelkow, E. M., Davies, P., and Mandelkow, E. (1998). A
943 nucleated assembly mechanism of Alzheimer paired helical filaments. *Proceedings of the*
944 *National Academy of Sciences of the United States of America*, *95*(26), 15712–15717.
945 https://doi.org/10.1073/pnas.95.26.15712
946 ▪ Frøkjaer-Jensen, C., Davis, M. W., Hopkins, C. E., Newman, B. J., Thummel, J. M., Olesen,
947 S. P., Grunnet, M., and Jorgensen, E. M. (2008). Single-copy insertion of transgenes in
948 Caenorhabditis elegans. *Nature genetics*, *40*(11), 1375–1383.
949 https://doi.org/10.1038/ng.248
950 ▪ Frost, B., and Diamond, M. I. (2010). Prion-like mechanisms in neurodegenerative diseases.
951 *Nature reviews. Neuroscience*, *11*(3), 155–159. https://doi.org/10.1038/nrn2786
952 ▪ Fu, H., Hussaini, S. A., Wegmann, S., Profaci, C., Daniels, J. D., Herman, M., Emrani, S.,
953 Figueroa, H. Y., Hyman, B. T., Davies, P., and Duff, K. E. (2016). 3D Visualization of the
954 Temporal and Spatial Spread of Tau Pathology Reveals Extensive Sites of Tau
955 Accumulation Associated with Neuronal Loss and Recognition Memory Deficit in Aged Tau
956 Transgenic Mice. *PloS one*, *11*(7), e0159463. https://doi.org/10.1371/journal.pone.0159463
957 ▪ Gao, S., Guan, S. A., Fouad, A. D., Meng, J., Kawano, T., Huang, Y. C., Li, Y., Alcaire, S.,
958 Hung, W., Lu, Y., Qi, Y. B., Jin, Y., Alkema, M., Fang-Yen, C., and Zhen, M. (2018).
959 Excitatory motor neurons are local oscillators for backward locomotion. *eLife*, *7*, e29915.
960 https://doi.org/10.7554/eLife.29915
961 ▪ Garriga, G., Desai, C., and Horvitz, H. R. (1993). Cell interactions control the direction of
962 outgrowth, branching and fasciculation of the HSN axons of Caenorhabditis elegans.
963 *Development (Cambridge, England)*, *117*(3), 1071–1087.
964 https://doi.org/10.1242/dev.117.3.1071
965 ▪ Ghoshal, N., García-Sierra, F., Wuu, J., Leurgans, S., Bennett, D. A., Berry, R. W., and
966 Binder, L. I. (2002). Tau conformational changes correspond to impairments of episodic
967 memory in mild cognitive impairment and Alzheimer's disease. *Experimental neurology*,
968 *177*(2), 475–493. https://doi.org/10.1006/exnr.2002.8014
969 ▪ Goedert, M., Baur, C. P., Ahringer, J., Jakes, R., Hasegawa, M., Spillantini, M. G., Smith, M.
970 J., and Hill, F. (1996). PTL-1, a microtubule-associated protein with tau-like repeats from the
971 nematode Caenorhabditis elegans. *Journal of cell science*, *109 (Pt 11)*, 2661–2672.
972 https://doi.org/10.1242/jcs.109.11.2661

973 ▪ Gordon, P., Hingula, L., Krasny, M. L., Swienckowski, J. L., Pokrywka, N. J., and Raley-
974 Susman, K. M. (2008). The invertebrate microtubule-associated protein PTL-1 functions in
975 mechanosensation and development in Caenorhabditis elegans. *Development genes and*
976 *evolution*, *218*(10), 541–551. https://doi.org/10.1007/s00427-008-0250-z
977 ▪ Grundke-Iqbal, I., Iqbal, K., Quinlan, M., Tung, Y. C., Zaidi, M. S., and Wisniewski, H. M.
978 (1986). Microtubule-associated protein tau. A component of Alzheimer paired helical
979 filaments. *The Journal of biological chemistry*, *261*(13), 6084–6089.
980 ▪ Harterink, M., Edwards, S. L., de Haan, B., Yau, K. W., van den Heuvel, S., Kapitein, L. C.,
981 Miller, K. G., and Hoogenraad, C. C. (2018). Local microtubule organization promotes cargo
982 transport in *C. elegans* dendrites. *Journal of cell science*, *131*(20), jcs223107.
983 https://doi.org/10.1242/jcs.223107
984 ▪ Hashi, Y., Kotani, S., and Adachi, T. (2016). A nematode microtubule-associated protein,
985 PTL-1, closely resembles its mammalian counterparts in overall molecular architecture.
986 *Bioscience, Biotechnology, and Biochemistry*, *80*(6), 1107–1113.
987 https://doi.org/10.1080/09168451.2016.1141038
988 ▪ Horvitz H. R. (2003). Worms, life, and death (Nobel lecture). *Chembiochem : a European*
989 *journal of chemical biology*, *4*(8), 697–711. https://doi.org/10.1002/cbic.200300614
990 ▪ Huang, Y., Liu, X. Q., Wyss-Coray, T., Brecht, W. J., Sanan, D. A., and Mahley, R. W.
991 (2001). Apolipoprotein E fragments present in Alzheimer's disease brains induce
992 neurofibrillary tangle-like intracellular inclusions in neurons. *Proceedings of the National*
993 *Academy of Sciences of the United States of America*, *98*(15), 8838–8843.
994 https://doi.org/10.1073/pnas.151254698
995 ▪ Iba, M., Guo, J. L., McBride, J. D., Zhang, B., Trojanowski, J. Q., and Lee, V. M. (2013).
996 Synthetic tau fibrils mediate transmission of neurofibrillary tangles in a transgenic mouse
997 model of Alzheimer's-like tauopathy. *The Journal of neuroscience : the official journal of the*
998 *Society for Neuroscience*, *33*(3), 1024–1037. https://doi.org/10.1523/JNEUROSCI.2642-
999 12.2013
1000 ▪ Izquierdo, E. J., and Beer, R. D. (2018). From head to tail: a neuromechanical model of
1001 forward locomotion in *Caenorhabditis elegans*. *Philosophical transactions of the Royal*
1002 *Society of London. Series B, Biological sciences*, *373*(1758), 20170374.
1003 https://doi.org/10.1098/rstb.2017.0374
1004 ▪ Jeganathan, S., Hascher, A., Chinnathambi, S., Biernat, J., Mandelkow, E. M., and
1005 Mandelkow, E. (2008). Proline-directed pseudo-phosphorylation at AT8 and PHF1 epitopes
1006 induces a compaction of the paperclip folding of Tau and generates a pathological (MC-1)
1007 conformation. *The Journal of biological chemistry*, *283*(46), 32066–32076.
1008 https://doi.org/10.1074/jbc.M805300200

1009 ▪ Jeganathan, S., von Bergen, M., Brutlach, H., Steinhoff, H. J., and Mandelkow, E. (2006).
1010 Global hairpin folding of tau in solution. *Biochemistry*, *45*(7), 2283–2293.
1011 https://doi.org/10.1021/bi0521543
1012 ▪ Jiang, W. I., Cao, Y., Xue, Y., Ji, Y., Winer, B. Y., Chandra, R., Zhang, X. F., Zhang, M.,
1013 Singhal, N. S., Pierce, J. T., Chen, S., and Ma, D. K. (2025). Suppressing APOE4-induced
1014 neural pathologies by targeting the VHL-HIF axis. *Proceedings of the National Academy of*
1015 *Sciences of the United States of America*, *122*(5), e2417515122.
1016 https://doi.org/10.1073/pnas.2417515122
1017 ▪ Kfoury, N., Holmes, B. B., Jiang, H., Holtzman, D. M., and Diamond, M. I. (2012). Trans-
1018 cellular propagation of Tau aggregation by fibrillar species. *The Journal of biological*
1019 *chemistry*, *287*(23), 19440–19451. https://doi.org/10.1074/jbc.M112.346072
1020 ▪ Köpke, E., Tung, Y. C., Shaikh, S., Alonso, A. C., Iqbal, K., and Grundke-Iqbal, I. (1993).
1021 Microtubule-associated protein tau. Abnormal phosphorylation of a non-paired helical
1022 filament pool in Alzheimer disease. *The Journal of biological chemistry*, *268*(32), 24374–
1023 24384.
1024 ▪ Koriath, C., Lashley, T., Taylor, W., Druyeh, R., Dimitriadis, A., Denning, N., Williams, J.,
1025 Warren, J. D., Fox, N. C., Schott, J. M., Rowe, J. B., Collinge, J., Rohrer, J. D., and Mead,
1026 S. (2019). ApoE4 lowers age at onset in patients with frontotemporal dementia and
1027 tauopathy independent of amyloid-β copathology. *Alzheimer's and dementia (Amsterdam,*
1028 *Netherlands)*, *11*, 277–280. https://doi.org/10.1016/j.dadm.2019.01.010
1029 ▪ Kosik, K. S., Orecchio, L. D., Binder, L., Trojanowski, J. Q., Lee, V. M., and Lee, G. (1988).
1030 Epitopes that span the tau molecule are shared with paired helical filaments. *Neuron*, *1*(9),
1031 817–825. https://doi.org/10.1016/0896-6273(88)90129-8
1032 ▪ Koutsodendris, N., Blumenfeld, J., Agrawal, A., Traglia, M., Grone, B., Zilberter, M., Yip, O.,
1033 Rao, A., Nelson, M. R., Hao, Y., Thomas, R., Yoon, S. Y., Arriola, P., and Huang, Y. (2023).
1034 Neuronal APOE4 removal protects against tau-mediated gliosis, neurodegeneration and
1035 myelin deficits. *Nature aging*, *3*(3), 275–296. https://doi.org/10.1038/s43587-023-00368-3
1036 ▪ Kowall, N. W., and Kosik, K. S. (1987). Axonal disruption and aberrant localization of tau
1037 protein characterize the neuropil pathology of Alzheimer's disease. *Annals of neurology*,
1038 *22*(5), 639–643. https://doi.org/10.1002/ana.410220514
1039 ▪ Kraemer, B. C., Zhang, B., Leverenz, J. B., Thomas, J. H., Trojanowski, J. Q., and
1040 Schellenberg, G. D. (2003). Neurodegeneration and defective neurotransmission in a
1041 Caenorhabditis elegans model of tauopathy. *Proceedings of the National Academy of*
1042 *Sciences of the United States of America*, *100*(17), 9980–9985.
1043 https://doi.org/10.1073/pnas.1533448100

1044 ▪ Krieg, M., Stühmer, J., Cueva, J. G., Fetter, R., Spilker, K., Cremers, D., Shen, K., Dunn, A.
1045 R., and Goodman, M. B. (2017). Genetic defects in β-spectrin and tau sensitize *C. elegans*
1046 axons to movement-induced damage via torque-tension coupling. *eLife*, *6*, e20172.
1047 https://doi.org/10.7554/eLife.20172
1048 ▪ Larsen, F. K., Baksh, R. A., McGlinchey, E., Langballe, E. M., Benejam, B., Beresford-
1049 Webb, J., McCarron, M., Coppus, A., Falquero, S., Fortea, J., Levin, J., Loosli, S. V., Mark,
1050 R., Rebillat, A. S., Zaman, S., and Strydom, A. (2024). Age of Alzheimer's disease diagnosis
1051 in people with Down syndrome and associated factors: Results from the Horizon 21
1052 European Down syndrome consortium. *Alzheimer's and dementia : the journal of the*
1053 *Alzheimer's Association*, *20*(5), 3270–3280. https://doi.org/10.1002/alz.13779
1054 ▪ Lee, S., Viqar, F., Zimmerman, M. E., Narkhede, A., Tosto, G., Benzinger, T. L., Marcus, D.
1055 S., Fagan, A. M., Goate, A., Fox, N. C., Cairns, N. J., Holtzman, D. M., Buckles, V., Ghetti,
1056 B., McDade, E., Martins, R. N., Saykin, A. J., Masters, C. L., Ringman, J. M., Ryan, N. S., …
1057 Dominantly Inherited Alzheimer Network (2016). White matter hyperintensities are a core
1058 feature of Alzheimer's disease: Evidence from the dominantly inherited Alzheimer network.
1059 *Annals of neurology*, *79*(6), 929–939. https://doi.org/10.1002/ana.24647
1060 ▪ Lee, V. M., and Trojanowski, J. Q. (1992). The disordered neuronal cytoskeleton in
1061 Alzheimer's disease. *Current opinion in neurobiology*, *2*(5), 653–656.
1062 https://doi.org/10.1016/0959-4388(92)90034-i
1063 ▪ Leroy, K., Yilmaz, Z., and Brion, J. P. (2007). Increased level of active GSK-3beta in
1064 Alzheimer's disease and accumulation in argyrophilic grains and in neurones at different
1065 stages of neurofibrillary degeneration. *Neuropathology and applied neurobiology*, *33*(1), 43–
1066 55. https://doi.org/10.1111/j.1365-2990.2006.00795.x
1067 ▪ Li, W., Kang, L., Piggott, B. J., Feng, Z., and Xu, X. Z. (2011). The neural circuits and
1068 sensory channels mediating harsh touch sensation in Caenorhabditis elegans. *Nature*
1069 *communications*, *2*, 315. https://doi.org/10.1038/ncomms1308
1070 ▪ Lima-Silva, T. B., Bahia, V. S., Carvalho, V. A., Guimarães, H. C., Caramelli, P., Balthazar,
1071 M., Damasceno, B., Bottino, C. M. C., Brucki, S. M. D., Nitrini, R., and Yassuda, M. S.
1072 (2013). Functional profile of patients with behavioral variant frontotemporal dementia
1073 (bvFTD) compared to patients with Alzheimer's disease and normal controls. *Dementia and*
1074 *neuropsychologia*, *7*(1), 96–103. https://doi.org/10.1590/S1980-57642013DN70100015
1075 ▪ Lin, L. C., Nana, A. L., Hepker, M., Hwang, J. L., Gaus, S. E., Spina, S., Cosme, C. G., Gan,
1076 L., Grinberg, L. T., Geschwind, D. H., Coppola, G., Rosen, H. J., Miller, B. L., and Seeley,
1077 W. W. (2019). Preferential tau aggregation in von Economo neurons and fork cells in
1078 frontotemporal lobar degeneration with specific MAPT variants. *Acta neuropathologica*
1079 *communications*, *7*(1), 159. https://doi.org/10.1186/s40478-019-0809-0

1080 ▪ Liu, L., Drouet, V., Wu, J. W., Witter, M. P., Small, S. A., Clelland, C., and Duff, K. (2012).
1081 Trans-synaptic spread of tau pathology in vivo. *PloS one*, *7*(2), e31302.
1082 https://doi.org/10.1371/journal.pone.0031302
1083 ▪ McCulloch, K. A., Qi, Y. B., Takayanagi-Kiya, S., Jin, Y., and Cherra, S. J., 3rd (2017). Novel
1084 Mutations in Synaptic Transmission Genes Suppress Neuronal Hyperexcitation in
1085 *Caenorhabditis elegans*. *G3 (Bethesda, Md.)*, *7*(7), 2055–2063.
1086 https://doi.org/10.1534/g3.117.042598
1087 ▪ McDermott, J. B., Aamodt, S., and Aamodt, E. (1996). ptl-1, a Caenorhabditis elegans gene
1088 whose products are homologous to the tau microtubule-associated proteins. *Biochemistry*,
1089 *35*(29), 9415–9423. https://doi.org/10.1021/bi952646n
1090 ▪ Meijering, E., Jacob, M., Sarria, J. C., Steiner, P., Hirling, H., and Unser, M. (2004). Design
1091 and validation of a tool for neurite tracing and analysis in fluorescence microscopy images.
1092 *Cytometry. Part A : the journal of the International Society for Analytical Cytology*, *58*(2),
1093 167–176. https://doi.org/10.1002/cyto.a.20022
1094 ▪ Meisl, G., Hidari, E., Allinson, K., Rittman, T., DeVos, S. L., Sanchez, J. S., Xu, C. K., Duff,
1095 K. E., Johnson, K. A., Rowe, J. B., Hyman, B. T., Knowles, T. P. J., and Klenerman, D.
1096 (2021). In vivo rate-determining steps of tau seed accumulation in Alzheimer's disease.
1097 *Science advances*, *7*(44), eabh1448. https://doi.org/10.1126/sciadv.abh1448
1098 ▪ Miller, K. G., Alfonso, A., Nguyen, M., Crowell, J. A., Johnson, C. D., and Rand, J. B. (1996).
1099 A genetic selection for Caenorhabditis elegans synaptic transmission mutants. *Proceedings*
1100 *of the National Academy of Sciences of the United States of America*, *93*(22), 12593–12598.
1101 https://doi.org/10.1073/pnas.93.22.12593
1102 ▪ Mitchell, D. H., Stiles, J. W., Santelli, J., and Sanadi, D. R. (1979). Synchronous growth and
1103 aging of Caenorhabditis elegans in the presence of fluorodeoxyuridine. *Journal of*
1104 *gerontology*, *34*(1), 28–36. https://doi.org/10.1093/geronj/34.1.28
1105 ▪ Mizumoto, K., and Shen, K. (2013). Interaxonal interaction defines tiled presynaptic
1106 innervation in C. elegans. *Neuron*, *77*(4), 655–666.
1107 https://doi.org/10.1016/j.neuron.2012.12.031
1108 ▪ Mocanu, M. M., Nissen, A., Eckermann, K., Khlistunova, I., Biernat, J., Drexler, D., Petrova,
1109 O., Schönig, K., Bujard, H., Mandelkow, E., Zhou, L., Rune, G., and Mandelkow, E. M.
1110 (2008). The potential for beta-structure in the repeat domain of tau protein determines
1111 aggregation, synaptic decay, neuronal loss, and coassembly with endogenous Tau in
1112 inducible mouse models of tauopathy. *The Journal of neuroscience : the official journal of*
1113 *the Society for Neuroscience*, *28*(3), 737–748. https://doi.org/10.1523/JNEUROSCI.2824-
1114 07.2008

1115 ▪ Natale, C., Barzago, M. M., and Diomede, L. (2020). *Caenorhabditis elegans* Models to
1116 Investigate the Mechanisms Underlying Tau Toxicity in Tauopathies. *Brain sciences*, *10*(11),
1117 838. https://doi.org/10.3390/brainsci10110838
1118 ▪ Nikoletopoulou, V., and Tavernarakis, N. (2014). Necrotic cell death in Caenorhabditis
1119 elegans. *Methods in enzymology*, *545*, 127–155. https://doi.org/10.1016/B978-0-12-801430-
1120 1.00006-8
1121 ▪ Nordquist, S. K., Smith, S. R., and Pierce, J. T. (2018). Systematic Functional
1122 Characterization of Human 21st Chromosome Orthologs in *Caenorhabditis elegans*. *G3*
1123 *(Bethesda, Md.)*, *8*(3), 967–979. https://doi.org/10.1534/g3.118.200019
1124 ▪ Nuriel, T., Angulo, S. L., Khan, U., Ashok, A., Chen, Q., Figueroa, H. Y., Emrani, S., Liu, L.,
1125 Herman, M., Barrett, G., Savage, V., Buitrago, L., Cepeda-Prado, E., Fung, C., Goldberg, E.,
1126 Gross, S. S., Hussaini, S. A., Moreno, H., Small, S. A., and Duff, K. E. (2017). Neuronal
1127 hyperactivity due to loss of inhibitory tone in APOE4 mice lacking Alzheimer's disease-like
1128 pathology. *Nature communications*, *8*(1), 1464. https://doi.org/10.1038/s41467-017-01444-0
1129 ▪ Oakley, S. S., Maina, M. B., Marshall, K. E., Al-Hilaly, Y. K., Harrington, C. R., Wischik, C.
1130 M., and Serpell, L. C. (2020). Tau Filament Self-Assembly and Structure: Tau as a
1131 Therapeutic Target. *Frontiers in neurology*, *11*, 590754.
1132 https://doi.org/10.3389/fneur.2020.590754
1133 ▪ O'Hagan, R., Chalfie, M., and Goodman, M. B. (2005). The MEC-4 DEG/ENaC channel of
1134 Caenorhabditis elegans touch receptor neurons transduces mechanical signals. *Nature*
1135 *neuroscience*, *8*(1), 43–50. https://doi.org/10.1038/nn1362
1136 ▪ Rietdijk, C. D., Perez-Pardo, P., Garssen, J., van Wezel, R. J., and Kraneveld, A. D. (2017).
1137 Exploring Braak's Hypothesis of Parkinson's Disease. *Frontiers in neurology*, *8*, 37.
1138 https://doi.org/10.3389/fneur.2017.00037
1139 ▪ Roberson, E. D., Scearce-Levie, K., Palop, J. J., Yan, F., Cheng, I. H., Wu, T., Gerstein, H.,
1140 Yu, G. Q., and Mucke, L. (2007). Reducing endogenous tau ameliorates amyloid beta-
1141 induced deficits in an Alzheimer's disease mouse model. *Science (New York, N.Y.)*,
1142 *316*(5825), 750–754. https://doi.org/10.1126/science.1141736
1143 ▪ Robinson, J. L., Lee, E. B., Xie, S. X., Rennert, L., Suh, E., Bredenberg, C., Caswell, C.,
1144 Van Deerlin, V. M., Yan, N., Yousef, A., Hurtig, H. I., Siderowf, A., Grossman, M., McMillan,
1145 C. T., Miller, B., Duda, J. E., Irwin, D. J., Wolk, D., Elman, L., McCluskey, L., … Trojanowski,
1146 J. Q. (2018). Neurodegenerative disease concomitant proteinopathies are prevalent, age-
1147 related and APOE4-associated. *Brain : a journal of neurology*, *141*(7), 2181–2193.
1148 https://doi.org/10.1093/brain/awy146
1149 ▪ Rohn, T. T., Catlin, L. W., Coonse, K. G., and Habig, J. W. (2012). Identification of an
1150 amino-terminal fragment of apolipoprotein E4 that localizes to neurofibrillary tangles of the

1151 Alzheimer's disease brain. *Brain research*, *1475*, 106–115.
1152 https://doi.org/10.1016/j.brainres.2012.08.003
1153 ▪ Rondina, J. M., Ferreira, L. K., de Souza Duran, F. L., Kubo, R., Ono, C. R., Leite, C. C.,
1154 Smid, J., Nitrini, R., Buchpiguel, C. A., and Busatto, G. F. (2017). Selecting the most
1155 relevant brain regions to discriminate Alzheimer's disease patients from healthy controls
1156 using multiple kernel learning: A comparison across functional and structural imaging
1157 modalities and atlases. *NeuroImage. Clinical*, *17*, 628–641.
1158 https://doi.org/10.1016/j.nicl.2017.10.026
1159 ▪ Rosen, H. J., Allison, S. C., Schauer, G. F., Gorno-Tempini, M. L., Weiner, M. W., and Miller,
1160 B. L. (2005). Neuroanatomical correlates of behavioural disorders in dementia. *Brain : a*
1161 *journal of neurology*, *128*(Pt 11), 2612–2625. https://doi.org/10.1093/brain/awh628
1162 ▪ Roux, A. E., Yuan, H., Podshivalova, K., Hendrickson, D., Kerr, R., Kenyon, C., and Kelley,
1163 D. (2023). Individual cell types in C. elegans age differently and activate distinct cell-
1164 protective responses. *Cell reports*, *42*(8), 112902.
1165 https://doi.org/10.1016/j.celrep.2023.112902
1166 ▪ Ryan, N. S., and Rossor, M. N. (2010). Correlating familial Alzheimer's disease gene
1167 mutations with clinical phenotype. *Biomarkers in medicine*, *4*(1), 99–112.
1168 https://doi.org/10.2217/bmm.09.92
1169 ▪ Sae-Lee, W., Scott, L. L., Brose, L., Encarnacion, A. J., Shi, T., Kore, P., Oyibo, L. O., Ye,
1170 C., Rozmiarek, S. K., and Pierce, J. T. (2020). *APP*-Induced Patterned Neurodegeneration
1171 Is Exacerbated by *APOE4* in *Caenorhabditis elegans*. *G3 (Bethesda, Md.)*, *10*(8), 2851–
1172 2861. https://doi.org/10.1534/g3.120.401486
1173 ▪ Sanfeliu-Cerdán, N., Català-Castro, F., Mateos, B., Garcia-Cabau, C., Ribera, M., Ruider, I.,
1174 Porta-de-la-Riva, M., Canals-Calderón, A., Wieser, S., Salvatella, X., and Krieg, M. (2023).
1175 A MEC-2/stomatin condensate liquid-to-solid phase transition controls neuronal
1176 mechanotransduction during touch sensing. *Nature cell biology*, *25*(11), 1590–1599.
1177 https://doi.org/10.1038/s41556-023-01247-0
1178 ▪ Santarella, R. A., Skiniotis, G., Goldie, K. N., Tittmann, P., Gross, H., Mandelkow, E. M.,
1179 Mandelkow, E., and Hoenger, A. (2004). Surface-decoration of microtubules by human tau.
1180 *Journal of molecular biology*, *339*(3), 539–553. https://doi.org/10.1016/j.jmb.2004.04.008
1181 ▪ Scahill, R. I., Schott, J. M., Stevens, J. M., Rossor, M. N., and Fox, N. C. (2002). Mapping
1182 the evolution of regional atrophy in Alzheimer's disease: unbiased analysis of fluid-
1183 registered serial MRI. *Proceedings of the National Academy of Sciences of the United*
1184 *States of America*, *99*(7), 4703–4707. https://doi.org/10.1073/pnas.052587399
1185 ▪ Schafer W. R. (2005). Egg-laying. *WormBook : the online review of C. elegans biology*, 1–7.
1186 https://doi.org/10.1895/wormbook.1.38.1

1187 ▪ Scharf, A., Pohl, F., Egan, B. M., Kocsisova, Z., and Kornfeld, K. (2021). Reproductive Aging
1188 in *Caenorhabditis elegans*: From Molecules to Ecology. *Frontiers in cell and developmental*
1189 *biology*, *9*, 718522. https://doi.org/10.3389/fcell.2021.718522
1190 ▪ Schneider, C. A., Rasband, W. S., and Eliceiri, K. W. (2012). NIH Image to ImageJ: 25 years
1191 of image analysis. *Nature Methods*, *9*(7), 671–675. doi:10.1038/nmeth.2089
1192 ▪ Seo, D. O., O'Donnell, D., Jain, N., Ulrich, J. D., Herz, J., Li, Y., Lemieux, M., Cheng, J., Hu,
1193 H., Serrano, J. R., Bao, X., Franke, E., Karlsson, M., Meier, M., Deng, S., Desai, C., Dodiya,
1194 H., Lelwala-Guruge, J., Handley, S. A., Kipnis, J., … Holtzman, D. M. (2023). ApoE isoform-
1195 and microbiota-dependent progression of neurodegeneration in a mouse model of
1196 tauopathy. *Science (New York, N.Y.)*, *379*(6628), eadd1236.
1197 https://doi.org/10.1126/science.add1236
1198 ▪ Serrano-Pozo, A., Das, S., and Hyman, B. T. (2021). APOE and Alzheimer's disease:
1199 advances in genetics, pathophysiology, and therapeutic approaches. *The Lancet.*
1200 *Neurology*, *20*(1), 68–80. https://doi.org/10.1016/S1474-4422(20)30412-9
1201 ▪ Shi, Y., Yamada, K., Liddelow, S. A., Smith, S. T., Zhao, L., Luo, W., Tsai, R. M., Spina, S.,
1202 Grinberg, L. T., Rojas, J. C., Gallardo, G., Wang, K., Roh, J., Robinson, G., Finn, M. B.,
1203 Jiang, H., Sullivan, P. M., Baufeld, C., Wood, M. W., Sutphen, C., … Holtzman, D. M.
1204 (2017). ApoE4 markedly exacerbates tau-mediated neurodegeneration in a mouse model of
1205 tauopathy. *Nature*, *549*(7673), 523–527. https://doi.org/10.1038/nature24016
1206 ▪ Spittaels, K., Van den Haute, C., Van Dorpe, J., Bruynseels, K., Vandezande, K., Laenen, I.,
1207 Geerts, H., Mercken, M., Sciot, R., Van Lommel, A., Loos, R., and Van Leuven, F. (1999).
1208 Prominent axonopathy in the brain and spinal cord of transgenic mice overexpressing four-
1209 repeat human tau protein. *The American journal of pathology*, *155*(6), 2153–2165.
1210 https://doi.org/10.1016/S0002-9440(10)65533-2
1211 ▪ Steciuk, M., Cheong, M., Waite, C., You, Y. J., and Avery, L. (2014). Regulation of synaptic
1212 transmission at the Caenorhabditis elegans M4 neuromuscular junction by an antagonistic
1213 relationship between two calcium channels. *G3 (Bethesda, Md.)*, *4*(12), 2535–2543.
1214 https://doi.org/10.1534/g3.114.014308
1215 ▪ Strang, K. H., Golde, T. E., and Giasson, B. I. (2019). MAPT mutations, tauopathy, and
1216 mechanisms of neurodegeneration. *Laboratory investigation; a journal of technical methods*
1217 *and pathology*, *99*(7), 912–928. https://doi.org/10.1038/s41374-019-0197-x
1218 ▪ Sündermann, F., Fernandez, M. P., and Morgan, R. O. (2016). An evolutionary roadmap to
1219 the microtubule-associated protein MAP Tau. *BMC genomics*, *17*, 264.
1220 https://doi.org/10.1186/s12864-016-2590-9
1221 ▪ Taylor, S. R., Santpere, G., Weinreb, A., Barrett, A., Reilly, M. B., Xu, C., Varol, E.,
1222 Oikonomou, P., Glenwinkel, L., McWhirter, R., Poff, A., Basavaraju, M., Rafi, I., Yemini, E.,

1223 Cook, S. J., Abrams, A., Vidal, B., Cros, C., Tavazoie, S., Sestan, N., … Miller, D. M., 3rd
1224 (2021). Molecular topography of an entire nervous system. *Cell*, *184*(16), 4329–4347.e23.
1225 https://doi.org/10.1016/j.cell.2021.06.023
1226 ▪ Therriault, J., Benedet, A. L., Pascoal, T. A., Mathotaarachchi, S., Chamoun, M., Savard, M.,
1227 Thomas, E., Kang, M. S., Lussier, F., Tissot, C., Parsons, M., Qureshi, M. N. I., Vitali, P.,
1228 Massarweh, G., Soucy, J. P., Rej, S., Saha-Chaudhuri, P., Gauthier, S., and Rosa-Neto, P.
1229 (2020). Association of Apolipoprotein E ε4 With Medial Temporal Tau Independent of
1230 Amyloid-β. *JAMA neurology*, *77*(4), 470–479. https://doi.org/10.1001/jamaneurol.2019.4421
1231 ▪ Topalidou, I., Chen, P. A., Cooper, K., Watanabe, S., Jorgensen, E. M., and Ailion, M.
1232 (2017). The NCA-1 and NCA-2 Ion Channels Function Downstream of G_q and Rho To
1233 Regulate Locomotion in *Caenorhabditis elegans*. *Genetics*, *206*(1), 265–282.
1234 https://doi.org/10.1534/genetics.116.198820
1235 ▪ Trent, C., Tsung, N., and Horvitz, H. R. (1983). Egg-laying defective mutants of the
1236 nematode Caenorhabditis elegans. *Genetics*, *104*(4), 619–647.
1237 https://doi.org/10.1093/genetics/104.4.619
1238 ▪ Trent, C., Tsung, N., and Horvitz, H. R. (1983). Egg-laying defective mutants of the
1239 nematode Caenorhabditis elegans. *Genetics*, *104*(4), 619–647.
1240 https://doi.org/10.1093/genetics/104.4.619
1241 ▪ Treusch, S., Hamamichi, S., Goodman, J. L., Matlack, K. E., Chung, C. Y., Baru, V.,
1242 Shulman, J. M., Parrado, A., Bevis, B. J., Valastyan, J. S., Han, H., Lindhagen-Persson, M.,
1243 Reiman, E. M., Evans, D. A., Bennett, D. A., Olofsson, A., DeJager, P. L., Tanzi, R. E.,
1244 Caldwell, K. A., Caldwell, G. A., … Lindquist, S. (2011). Functional links between Aβ toxicity,
1245 endocytic trafficking, and Alzheimer's disease risk factors in yeast. *Science (New York,*
1246 *N.Y.)*, *334*(6060), 1241–1245. https://doi.org/10.1126/science.1213210
1247 ▪ Trojanowski, J. Q., Schmidt, M. L., Shin, R. W., Bramblett, G. T., Rao, D., and Lee, V. M.
1248 (1993). Altered tau and neurofilament proteins in neuro-degenerative diseases: diagnostic
1249 implications for Alzheimer's disease and Lewy body dementias. *Brain pathology (Zurich,*
1250 *Switzerland)*, *3*(1), 45–54. https://doi.org/10.1111/j.1750-3639.1993.tb00725.x
1251 ▪ Tsutsui, K., Kim, H. S., Yoshikata, C., Kimura, K., Kubota, Y., Shibata, Y., Tian, C., Liu, J.,
1252 and Nishiwaki, K. (2021). Repulsive guidance molecule acts in axon branching in
1253 Caenorhabditis elegans. *Scientific reports*, *11*(1), 22370. https://doi.org/10.1038/s41598-
1254 021-01853-8
1255 ▪ Tuovinen, T., Kananen, J., Rajna, Z., Lieslehto, J., Korhonen, V., Rytty, R., Mattila, H.,
1256 Huotari, N., Raitamaa, L., Helakari, H., Elseoud, A. A., Krüger, J., LeVan, P., Tervonen, O.,
1257 Hennig, J., Remes, A. M., Nedergaard, M., and Kiviniemi, V. (2020). The variability of

1258 functional MRI brain signal increases in Alzheimer's disease at cardiorespiratory
1259 frequencies. *Scientific reports*, *10*(1), 21559. https://doi.org/10.1038/s41598-020-77984-1
1260 ▪ Vaccaro, A., Tauffenberger, A., Aggad, D., Rouleau, G., Drapeau, P., and Parker, J. A.
1261 (2012). Mutant TDP-43 and FUS cause age-dependent paralysis and neurodegeneration in
1262 C. elegans. *PloS one*, *7*(2), e31321. https://doi.org/10.1371/journal.pone.0031321
1263 ▪ van Ham, T. J., Thijssen, K. L., Breitling, R., Hofstra, R. M., Plasterk, R. H., and Nollen, E. A.
1264 (2008). C. elegans model identifies genetic modifiers of alpha-synuclein inclusion formation
1265 during aging. *PLoS genetics*, *4*(3), e1000027. https://doi.org/10.1371/journal.pgen.1000027
1266 ▪ Vidal-Gadea, A., Topper, S., Young, L., Crisp, A., Kressin, L., Elbel, E., Maples, T., Brauner,
1267 M., Erbguth, K., Axelrod, A., Gottschalk, A., Siegel, D., and Pierce-Shimomura, J. T. (2011).
1268 Caenorhabditis elegans selects distinct crawling and swimming gaits via dopamine and
1269 serotonin. *Proceedings of the National Academy of Sciences of the United States of*
1270 *America*, *108*(42), 17504–17509. https://doi.org/10.1073/pnas.1108673108
1271 ▪ Vogel, J. W., Iturria-Medina, Y., Strandberg, O. T., Smith, R., Levitis, E., Evans, A. C.,
1272 Hansson, O., Alzheimer’s Disease Neuroimaging Initiative, and Swedish BioFinder Study
1273 (2020). Spread of pathological tau proteins through communicating neurons in human
1274 Alzheimer's disease. *Nature communications*, *11*(1), 2612. https://doi.org/10.1038/s41467-
1275 020-15701-2
1276 ▪ Vogel, J. W., Iturria-Medina, Y., Strandberg, O. T., Smith, R., Levitis, E., Evans, A. C.,
1277 Hansson, O., Alzheimer’s Disease Neuroimaging Initiative, and Swedish BioFinder Study
1278 (2020). Spread of pathological tau proteins through communicating neurons in human
1279 Alzheimer's disease. *Nature communications*, *11*(1), 2612. https://doi.org/10.1038/s41467-
1280 020-15701-2
1281 ▪ Vossel, K. A., Zhang, K., Brodbeck, J., Daub, A. C., Sharma, P., Finkbeiner, S., Cui, B., and
1282 Mucke, L. (2010). Tau reduction prevents Abeta-induced defects in axonal transport.
1283 *Science (New York, N.Y.)*, *330*(6001), 198. https://doi.org/10.1126/science.1194653
1284 ▪ Way, J. C., and Chalfie, M. (1989). The mec-3 gene of Caenorhabditis elegans requires its
1285 own product for maintained expression and is expressed in three neuronal cell types. *Genes*
1286 *& development*, *3*(12A), 1823–1833. https://doi.org/10.1101/gad.3.12a.1823
1287 ▪ Wegmann, S., Maury, E. A., Kirk, M. J., Saqran, L., Roe, A., DeVos, S. L., Nicholls, S., Fan,
1288 Z., Takeda, S., Cagsal-Getkin, O., William, C. M., Spires-Jones, T. L., Pitstick, R., Carlson,
1289 G. A., Pooler, A. M., and Hyman, B. T. (2015). Removing endogenous tau does not prevent
1290 tau propagation yet reduces its neurotoxicity. *The EMBO journal*, *34*(24), 3028–3041.
1291 https://doi.org/10.15252/embj.201592748
1292 ▪ White, J. G., Southgate, E., Thomson, J. N., and Brenner, S. (1986). The structure of the
1293 nervous system of the nematode Caenorhabditis elegans. *Philosophical transactions of the*

1294 *Royal Society of London. Series B, Biological sciences*, *314*(1165), 1–340.
1295 https://doi.org/10.1098/rstb.1986.0056
1296 ▪ Wu, Z., Cardona, E. A., Cohn, J. A., and Pierce, J. T. (2025). Nonapoptotic role of EGL-1 in
1297 exopher production and neuronal health in *Caenorhabditis elegans*. *Proceedings of the*
1298 *National Academy of Sciences of the United States of America*, *122*(2), e2407909122.
1299 https://doi.org/10.1073/pnas.2407909122
1300 ▪ Wu, Z., Ghosh-Roy, A., Yanik, M. F., Zhang, J. Z., Jin, Y., and Chisholm, A. D. (2007).
1301 Caenorhabditis elegans neuronal regeneration is influenced by life stage, ephrin signaling,
1302 and synaptic branching. *Proceedings of the National Academy of Sciences of the United*
1303 *States of America*, *104*(38), 15132–15137. https://doi.org/10.1073/pnas.0707001104
1304 ▪ Yoshiyama, Y., Higuchi, M., Zhang, B., Huang, S. M., Iwata, N., Saido, T. C., Maeda, J.,
1305 Suhara, T., Trojanowski, J. Q., and Lee, V. M. (2007). Synapse loss and microglial activation
1306 precede tangles in a P301S tauopathy mouse model. *Neuron*, *53*(3), 337–351.
1307 https://doi.org/10.1016/j.neuron.2007.01.010
1308 ▪ Zhou, W., Scott, S. A., Shelton, S. B., and Crutcher, K. A. (2006). Cathepsin D-mediated
1309 proteolysis of apolipoprotein E: possible role in Alzheimer's disease. *Neuroscience*, *143*(3),
1310 689–701. https://doi.org/10.1016/j.neuroscience.2006.08.019
1311

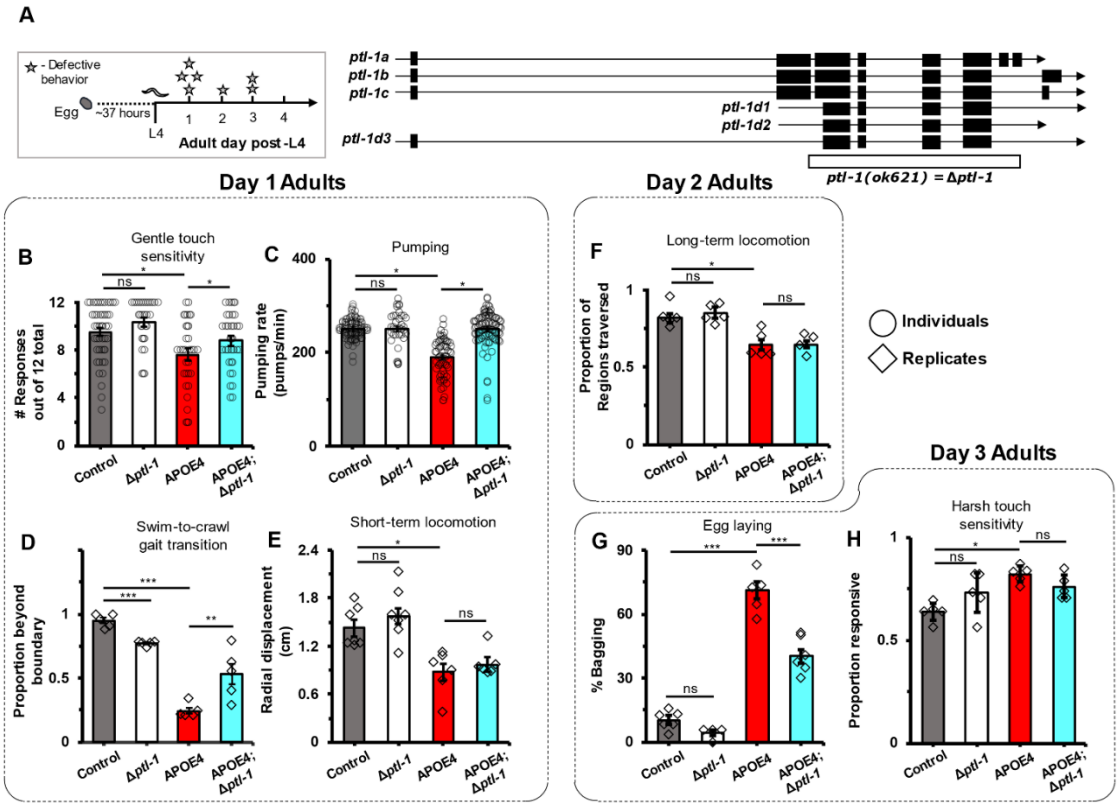

Figure 1. *ptl-1* is required for widespread, progressive neuronal dysfunction induced by APOE4.

(A left) Timeline from egg lay to the adult age of onset at which defective or abnormal performance in APOE4 versus control animals are first detected.

(A right) Endogenous *ptl-1* locus with all known isoforms and the portion deleted in the *ok621* allele as indicated below.

(B-H) Results of behavioral assays, used to proxy neuronal dysfunction, which are arranged by the adult age of onset for APOE4-induced defective or abnormal performance.

(B-E) D1 adult onset. (B) Subtle defect in gentle touch sensitivity which is fully suppressed by *ptl-1* deletion. N=47 for control, N=30 for Δ*ptl-1*, N=33 for APOE4, and N=35 for APOE4;Δ*ptl-1*. (C) Subtle defect in pharyngeal pumping which is fully suppressed by *ptl-1* deletion. N=94 for control, N=37 for Δ*ptl-1*, N=61 for APOE4, and N=91 for APOE4;Δ*ptl-1*. (D) Severe defect in swim-to-crawl gait transition which is partially suppressed by *ptl-1* deletion. N=164 control, N=136 for Δ*ptl-1*, N=162 for APOE4, N=165 for APOE4;Δ*ptl-1*. (E) Subtle defect in short-term locomotion which is not suppressed by *ptl-1* deletion. N=47 for control, N=38 for Δ*ptl-1*, N=44 for APOE4, and N=44 for APOE4;Δ*ptl-1*).

(F) D2 adult onset. Subtle defect in long-term locomotion which is not suppressed by *ptl-1* deletion. N=31 control, N=32 for Δ*ptl-1*, N=28 for APOE4, and N=29 for APOE4;Δ*ptl-1*.

(G,H) D3 adult onset. (G) Severe egg laying defect which is partially suppressed by *ptl-1* deletion. N=196 for control, N=134 for Δ*ptl-1*, N=214 for APOE4, N=243 for APOE4;Δ*ptl-1*. (H) Subtle, abnormal increase in harsh touch sensitivity. N=25 for control, N=17 for Δ*ptl-1*, N=26 for APOE4, and N=31 for APOE4;Δ*ptl-1*.

All data are represented as mean ± SEM. N is the total sample size representing all animals across replicates. Statistical comparisons were made using χ^2 tests of independence for D,G and Student's t-test for B,C,E,F,G. *: p<0.05; **: p<0.01; ***: p<0.001.

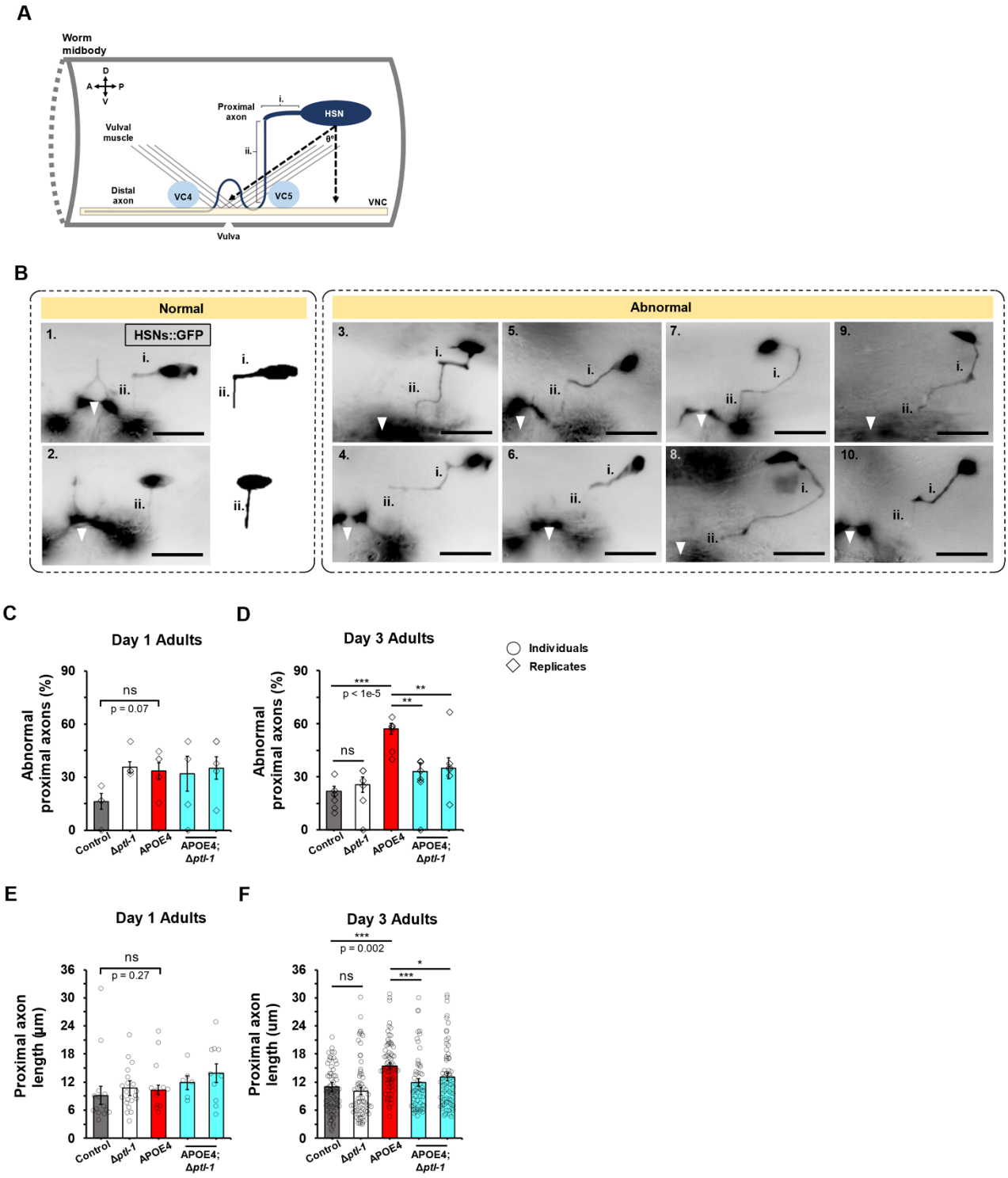
A
Worm midbody
D
A
P
V
Proximal axon
i.
HSN
Vulval muscle
ii.
θ°
Distal axon
VC4
VC5
VNC
Vulva
B
Normal
Abnormal
HSNs::GFP
1.
2.
3.
4.
5.
6.
7.
8.
9.
10.
C
Day 1 Adults
Abnormal proximal axons (%)
ns
p = 0.07
Control
Δptl-1
APOE4
APOE4; Δptl-1
D
Day 3 Adults
Abnormal proximal axons (%)
***
p < 1e-5
**
ns
Individuals
Replicates
E
Day 1 Adults
Proximal axon length (μm)
ns
p = 0.27
F
Day 3 Adults
Proximal axon length (um)
***
p = 0.002
*

Figure 2. *ptl-1* is required for APOE4-induced HSN axon degeneration.

(A) Cartoon of the worm midbody, centered about the vulva area, depicting: the HSN proximal axon, the VC4,5 neurons, vulval musculature, and ventral nerve cord (VNC).

(B) Representative live images of normal (1,2) and abnormal (3-10) HSN proximal axons visualized with GFP. Proximal axon segments are marked by i. and ii (with exception to image 2, where segment identity is less certain). The vulva area is also marked with a white arrowhead for anatomical reference. All scale bars are 20 μm.

(C,D) Percentage of animals with abnormal HSN proximal axons in D1 and D3 adults. The baseline incidence of abnormal axons in control was similar between D1 and D3.

(C) D1 adults. All other groups show non-significant, but slightly increased incidence of abnormal axons compared to control. N=37 for control, N=59 Δ*ptl-1*, N=51 for APOE4, N=22 for APOE4;Δ*ptl-1* (left), and N=37 for APOE4;Δ*ptl-1* (right).

(D) The incidence of abnormal axons appears to correlate with defective egg laying behavior (See Fig. 1G) in D3 adults. N=101 for control, N=78 for Δ*ptl-1*, N=91 for APOE4, N=79 for APOE4;Δ*ptl-1* (left), and N=86 for APOE4;Δ*ptl-1* (right).

(E,F) Quantification of HSN proximal axon lengths in D1 and D3 adults. The baseline axon length in control was similar between D1 and D3.

(E) D1 adults. Axon length was similar across all groups. N=15 for control, N=13 Δ*ptl-1*, N=20 for APOE4, N=6 for APOE4;Δ*ptl-1* (left), and N=10 for APOE4;Δ*ptl-1* (right).

(D) D3 adults. Axon length appears to correlate with the incidence of abnormal axons shown in (C) and defective egg laying behavior (See Fig. 1G). N=79 for control, N=66 for Δ*ptl-1*, N=72 for APOE4, N=54 for APOE4;Δ*ptl-1* (left), and N=66 for APOE4;Δ*ptl-1* (right).

All data are represented as mean ± SEM. N is the total sample size representing all animals across replicates. Statistical comparisons were made using χ^2 tests of independence for C and D and Student's t-test for (E) and (F). *: $p<0.05$; **: $p<0.01$; ***: $p<0.001$.

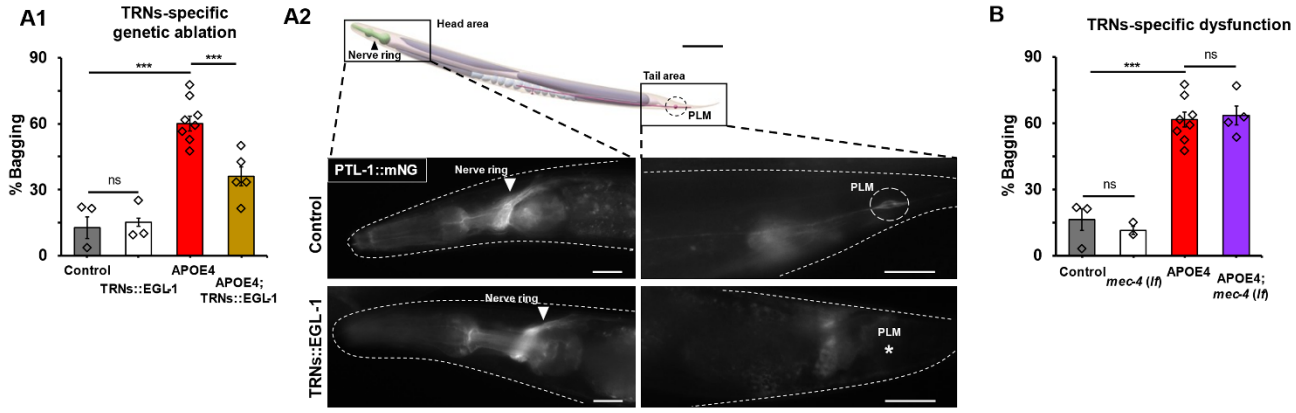

Figure 3. Targeted genetic ablation, but not abolished function, of the TRNs protects HSN against APOE4-induced dysfunction.

(A1) Egg-laying behavior across groups. Genetic ablation of the TRNs partially suppressed egg-laying defects in APOE4 animals as with the *ptl-1* deletion (See Fig. 1G). N=104 for control, N=171 for TRNs::EGL-1, N=525 for APOE4, and N=190 for APOE4;TRNs::EGL-1.

(A2 top) Cartoon depicting the head and tail areas wherein the nerve ring and PLM neuron, respectively, are located.

(A2 bottom) Representative live images of nerve ring (arrowhead) and PLM neuron (within dashed circle if present; marked with asterisk if absent) visualized with PTL-1::mNG in control and TRNs::EGL-1 animals. Dashed borders indicate the worm body outline. All scale bars are 20 µm.

(B) Egg-laying behavior across groups. In contrast to genetic ablation, abolishing TRN function did not suppress egg laying defects. N=104 for control, N=123 for *mec-4*(*lf*), N=525 for APOE4, and N=101 for APOE4;*mec-4*(*lf*) (left), and N=125 for APOE4;*mec-4*(*lf*) (right).

All data are represented as mean ± SEM. N is the total sample size representing all animals across replicates. All statistical comparisons were made using χ^2 tests of independence. control and APOE4 data are re-plotted in (A1) and (B). *: $p<0.05$; **: $p<0.01$; ***: $p<0.001$.

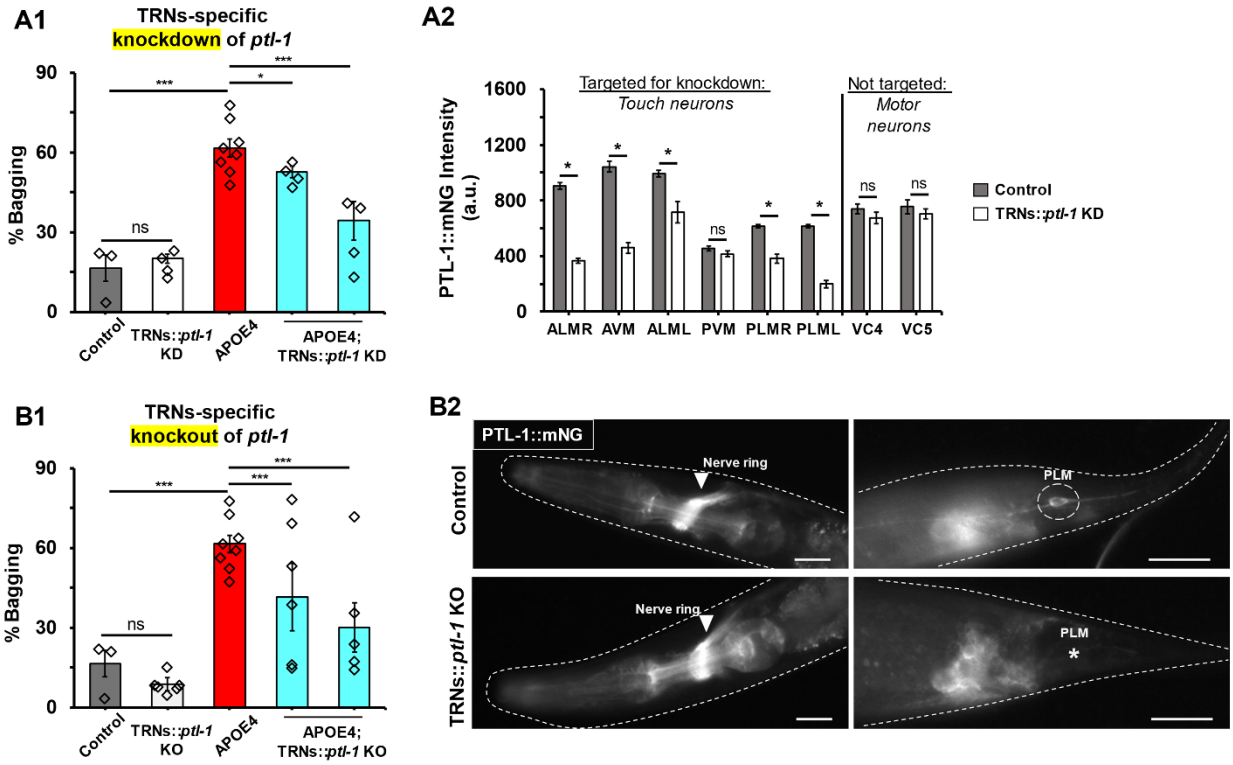

Figure 4. Targeted depletion of PTL-1 in the TRNs protects HSN against APOE4-induced dysfunction.

(A1) Egg-laying behavior across groups. N=104 for control, N=180 for TRNs::*ptl-1* KD, N=525 for APOE4, N=171 for APOE4;TRNs:: *ptl-1* KD (Left), and N=108 for APOE4;TRNs:: *ptl-1* KD (Right).

(A2) Quantification of *ptl-1* knockdown in the targeted TRNs and non-targeted VCs4,5 neurons between control and TRNs::*ptl-1* KD animals using PTL-1::mNG fluorescence intensity in the soma.

(B1) Egg-laying behavior across groups. N=104 for control, N=348 for TRNs::*ptl-1* KO, N=525 for APOE4, N=423 for APOE4;TRNs:: *ptl-1* KO (*Left*), and N=519 for APOE4;TRNs:: *ptl-1* KO (Right).

(B2) Representative live images of nerve ring (arrowhead) and PLM neuron (within dashed circle if present; area marked with asterisk if absent) visualized with PTL-1::mNG in control and TRNs::*ptl-1* KO animals. Dashed borders indicate the worm body outline. All scale bars are 20 µm.

All data are represented as mean ± SEM. N is the total sample size representing all animals across replicates. Statistical comparisons were made using χ^2 tests of independence for A1,B1 and Student's t-test for A2. Control and APOE4 data are re-plotted in (A1) and (B1). *: p<0.05; **: p<0.01; ***: p<0.001.